CHALMERS
UNIVERSITY OF TECHNOLOGY

State-Space Control of Electric Vehicle Charging

Optimal Control of an Integrated Three-Phase IPMSM-Based Boost Converter

Master's thesis in Automatic Control

Abukar Hassan

DEPARTMENT OF ELECTRICAL ENGINEERING
CHALMERS UNIVERSITY OF TECHNOLOGY
Gothenburg, Sweden 2026
www.chalmers.se

Master's Thesis in Automatic Control

State-Space Control of Electric Vehicle Charging

Optimal Control of an Integrated Three-Phase IPMSM-Based Boost Converter

Abukar Hassan

CHALMERS
UNIVERSITY OF TECHNOLOGY

Department of Electrical Engineering
Division of Automatic Control
Chalmers University of Technology
Gothenburg, Sweden 2026

State-Space Control of Electric Vehicle Charging
Optimal Control of an Integrated Three-Phase IPMSM-Based
Abukar Hassan

Supervisor: Peter Joseph, Volvo Cars
Examiner: Anders Grauers, Professor
Department of Electrical Engineering

Master's Thesis 2026
Department of Electrical Engineering
Division of Automatic Control
Chalmers University of Technology
SE-412 96 Gothenburg
Telephone +46 31 772 1000

Cover: The application area of the system developed in this thesis.

Typeset in LaTeX
Printed by Chalmers Reproservice
Gothenburg, Sweden 2026

State-Space Control of Electric Vehicle Charging
Optimal Control of an Integrated Three-Phase IPMSM-Based Boost Converter
Abukar Hassan
Department of Electrical Engineering
Chalmers University of Technology

Abstract

The increasing adoption of high-voltage battery systems in electric vehicles presents challenges when interfacing with legacy charging infrastructure designed for lower battery voltage levels. This is because the charging voltage must exceed the battery voltage to drive current into the battery pack. To address this, the stator windings of the electric machine are utilised as inductive elements within a DC–DC boost converter, thereby reducing additional hardware requirements and enabling effective voltage boosting.

However, employing the stator windings introduces significant control challenges due to nonlinear dynamics, rotor-angle-dependent inductance, magnetic coupling, and eddy current effects. These characteristics lead to phase coupling, parameter variation, and the risk of unintended torque generation. To overcome these issues, a state-space-based cascade control strategy is developed, comprising an inner current control loop and an outer voltage control loop, both incorporating integral action to ensure accurate tracking and elimination of steady-state error.

The charging system is modelled and controlled in Continuous Conduction Mode (CCM), which represents the dominant operating regime during charging.

The charging system is fundamentally control-affine with a state-dependent input matrix, which introduces nonlinear behaviour. The nonlinear system is linearised around a stable operating point using a first-order Taylor expansion and the Jacobian matrix, enabling controller synthesis. The inner-loop controller is designed using Linear Quadratic Regulator (LQR) techniques, while the outer-loop controller is tuned via pole placement. Model accuracy is validated through comparison with analytical transfer functions and independent circuit simulations, including verification of transient behaviour using resonance-based peak-to-peak analysis.

The proposed control framework is evaluated under varying operating conditions, including changes in supply voltage, load, and rotor position. The results demonstrate stable and reliable voltage boosting, effective current regulation, and robustness to system nonlinearities. Furthermore, the state-space formulation provides a flexible and adaptable control structure, supporting efficient integration into evolving system designs and reducing development effort for the OEM.

Keywords: Integrated on-board charger (IOBC), Electric vehicle charging, IPMSM, DC–DC boost converter, State-space control, Linear Quadratic Regulator (LQR), Cascade control, Continuous Conduction Mode (CCM).

Acknowledgements

I would like to express gratitude to the senior engineers whose expertise helped narrow the scope of my investigations and prevented me from pursuing unproductive avenues. Their guidance significantly reduced the time required to identify viable solutions.
In particular, I would like to thank Shayan Halder for his guidance on discretisation effects, induction-related topics, and numerous technical matters.
I am also grateful to Joachim Härsjö for reviewing parts of this work, identifying errors, and suggesting effective corrections.
Special thanks to Sharan Vasanadu for the insightful discussions regarding PWM implementation and the settling-time characteristics of the current controller.
I am grateful to Jithinal Kizakkayial for helping me identify an error in the circuit model at an early stage of the project, preventing considerable effort from being spent on an incorrect foundation.
I would like to thank my supervisor, Peter Joseph, for allowing me the freedom to work independently while providing support when needed. I am especially grateful for the base circuit model he provided, which formed the foundation for the validation of the system presented in this work.
Finally, I would like to extend my appreciation to my examiner, Anders Grauers, for consistently relating theoretical concepts to practical outcomes. His comments not only saved considerable time but also contributed to my understanding of the subject.

Abukar Hassan, Gothenburg, June 2026

List of Acronyms

Below is the list of acronyms that have been used throughout this thesis listed in alphabetical order:

AC	Alternating Current
BES	Battery Energy Storage
CCM	Continuous Conduction Mode
DC	Direct Current
DCM	Discontinuous Conduction Mode
EV	Electric Vehicle
IOBC	Integrated On-Board Charger
IPMSM	Interior Permanent Magnet Synchronous Motor
KCL	Kirchhoff's Current Law
KVL	Kirchhoff's Voltage Law
LQR	Linear Quadratic Regulator
LTI	Linear Time-Invariant
MIMO	Multiple-Input Multiple-Output
OBC	On-Board Charger
PI	Proportional-Integral
PWM	Pulse Width Modulation
SISO	Single-Input Single-Output
SOC	State of Charge

Nomenclature

Below is the nomenclature of indices, sets, parameters, and variables that have been used throughout this thesis.

Indices

a, b, c	Indices for individual three-phase stator windings
d, q	Indices for direct and quadrature axes in the synchronous reference frame
t	Index for continuous time step

Sets

$\mathcal{X}$	State space vector set
$\mathcal{U}$	Control input vector set

Parameters

C_{in}	Input capacitor capacitance [F]
C_{out}	Output capacitor capacitance [F]
f_{sw}	Power electronics switching frequency [Hz]
I_{station}	Constant charging station supply current [A]
L_{δ}	Saliency component inductance reference [H]
L_{ls}	Stator leakage inductance [H]
L_m	Mutual air-gap inductance [H]
p	Number of motor pole pairs [-]
P_{station}	Nominal charging station power [W]
R_{in}	Input cable and connector parasitic resistance [Ω]

R_{out}	DC-link cable resistance to the battery [Ω]
r_s	Stator copper coil winding resistance [Ω]
T_s	Sampling time interval [s]
$V_{\text{Battery}}, V_{\text{batt}}$	High-voltage traction battery terminal voltage [V]
V_{Station}, V_S	Charging station supply/input voltage [V]
$\bar{D}$	Nominal duty ratio operating point equilibrium
ψ_m, flux_m	Permanent magnet flux linkage reference [Wb]
$\bar{x}, \bar{u}$	Equilibrium operating points for states and control inputs
σ_n	Algebraic matrix simplification variables ($n = 1, 2, \ldots, 13$)

Variables

D_a, D_b, D_c	Phase duty cycle control inputs for inverter legs
$\boldsymbol{D}_{\text{abc}}$	Three-phase duty cycle input vector
i_a, i_b, i_c	Instantaneous currents in the three-phase stator windings [A]
$\boldsymbol{i}_{\text{abc}}$	Three-phase stator current vector
i_d, i_q	Direct and quadrature axis currents in the synchronous reference frame [A]
I_{sum}	Total summation of the active phase charging currents [A]
T_e	Parasitic electromagnetic torque generated in the air-gap [Nm]
$u(t), \Delta u$	System input vector and its small-signal perturbation deviation
$v_{C_{\text{in}}}, V_{\text{Cin}}$	Dynamic voltage across the input smoothing capacitor [V]
$v_{C_{\text{out}}}, V_{\text{Cout}}$	Dynamic voltage across the output smoothing capacitor [V]
$x(t), \Delta x$	State space vector and its small-signal perturbation deviation
$y(t), \Delta y$	System output tracking vector and its perturbation deviation
$z(t)$	Augmented state vector tracking the integral error
θ	Fixed rotor mechanical angle position during charging session [rad]
$\boldsymbol{L}_{\text{abc}}^{-1}(\theta)$	Position-dependent analytical inverse inductance matrix

Contents

List of Figures

List of Tables

1

Introduction

1.1 Background

Climate change has become pressing global concerns due to their harmful effects on ecosystems and human society. These impacts are primarily driven by greenhouse gas (GHG) emissions. The transport sector is a major contributor, accounting for around 20% of global carbon dioxide (CO_2) emissions, with road transport forming the largest share [3]. Electrification is widely regarded as one of the most effective ways to reduce reliance on fossil fuels and lower emissions. As electric vehicle (EV) adoption increases, there is growing demand for efficient charging systems and power electronic converters that ensure reliable energy transfer while minimising cost, weight, and energy losses.

EVs are increasingly adopting high-voltage battery architectures, such as 800 V systems, in order to enable faster charging, reduce current levels, and improve overall efficiency. However, much of the existing DC charging infrastructure is designed around a nominal voltage of approximately 400 V. To ensure compatibility between charging stations and high-voltage battery systems, EVs require an onboard DC–DC power conversion system. Conventional solutions typically rely on dedicated inductive components, which increase system size, cost, and weight. Therefore, there is growing interest in more integrated approaches in which existing electrical machine components are reused as part of the power electronic conversion system [4]. In this context, the stator windings of an interior permanent magnet synchronous machine (IPMSM) can be used as the inductive energy storage element in a three-phase boost converter. This approach enables a more compact system architecture by removing the need for external inductors, while making effective use of hardware already present in the vehicle, rather than adding additional components.

Although the use of IPMSM stator windings as boost inductors offers hardware advantages, it introduces complex control and modelling challenges. Unlike ideal inductors, the stator windings exhibit nonlinear and rotor-position-dependent behaviour due to magnetic saliency, saturation effects, and coupling with the rotor permanent magnet field [1]. These effects result in a nonlinear multi-input multi-output (MIMO) system with strong coupling between electrical phases and rotor position. Furthermore, current injection into the stator windings can generate unintended electromagnetic torque through interaction with the rotor magnetic field, meaning that the energy conversion process must be carefully controlled to avoid mechanical excitation [5].

1.2 Problem Statement

To charge the battery, the voltage supplied by the charging station must be increased to a level higher than the battery voltage. Using the IPMSM as part of the boost converter can reduce both material usage and system cost. However, this approach requires an appropriate control strategy. The controller must prevent unwanted torque production, limit current variation, and protect system components, particularly the capacitors, from overvoltage, that may lead to protective actions or emergency shutdowns.

1.3 Aim and Objectives

The main aim of this thesis is to develop and validate a state-space based cascade control strategy for a three-phase on board IPMSM based boost converter intended for high voltage battery charging in electric vehicles.
The objectives are:

- The development of a nonlinear dynamic model of the IPMSM-based boost charging system, incorporating rotor-angle-dependent inductance and magnetic coupling effects.
- The derivation of a linearised state-space representation around a selected operating point, enabling tractable control design.
- The design of a cascade control architecture comprising an inner current loop and an outer voltage loop, including integral action through state augmentation to eliminate steady-state error.
- The synthesis of the inner-loop controller using optimal state-space methods and the outer-loop controller using pole placement techniques.
- The validation of the proposed modelling and control approach using both analytical transfer function analysis and detailed circuit-level simulations under varying operating conditions.

1.4 Scope and Limitations

This work is restricted to continuous conduction mode (CCM), which constitutes the majority of the charging period, wherein the inductor current remains continuous throughout the switching cycle. The extension to discontinuous conduction mode (DCM), which typically occurs towards the end of the charging process and introduces additional nonlinearities and mode-dependent behaviour, lies outside the scope of this thesis and is left for future work.
High-frequency switching ripple is not directly controlled. Instead, the control strategy focuses on regulating the average values of current and voltage. State estimation techniques, such as Kalman filters, are also excluded from this work, as they may not be sufficiently fast for the rapid dynamics of high-frequency DC–DC conversion. Therefore, the approach adopted in this work assumes direct state measurement, necessitating reliable sensors with low measurement error.

1.5 Contributions

The main contributions of this work are as follows:

- The development of a nonlinear state-space model of a three-phase boost converter utilising IPMSM stator windings as inductive elements, including the incorporation of rotor-position-dependent inductance and magnetic coupling effects within the state-space formulation.
- The design of a cascade state-space control framework with integral action for voltage and current regulation.
- The application of convex optimisation techniques, specifically Linear Quadratic Regulator (LQR) tuning, for inner-loop current control, alongside pole placement methods for outer-loop voltage control.
- The validation of the proposed model and control strategy using both transfer function analysis and circuit-level simulations.
- The development of a modular modelling framework that can be extended to different phase configurations, including single-phase, two-phase, and three-phase operation.

2
Theory

2.1 Power Electronics & Booster Topology

2.1.1 The E-Machine Based DC-Booster Configuration

In the context of high-power electric vehicle charging, where a DC fast-charging station must supply a high-voltage traction battery, a conventional boost stage can be realised in a more integrated manner. Instead of employing discrete inductors, the stator windings of the electric machine are utilised as the energy-storage elements of the DC-DC boost converter. This approach enables a significant reduction in system mass, volume, and component count, while improving functional integration within the drivetrain [4].
Boost converters operate in a straightforward manner, in which current is driven through an inductor and subsequently reshaped by rapidly switching. During the on state the switch connects the inductor to ground, allowing current to ramp up. During the off state, the switch opens and current is forced through the diode to the output capacitor and load [6]. This switching action exploits the inherent property of an inductor to resist changes in current. When the current is interrupted or redirected, the inductor generates a back electromotive force (EMF) due to the collapsing magnetic field, in accordance with Faraday's law [7], see Equation 2.1. This induced voltage increases significantly during the switching transitions, effectively transferring stored magnetic energy into the electrical domain.

$$\mathcal{E} = -N\frac{d\Phi}{dt} = -L\frac{di}{dt} \tag{2.1}$$

Where:

- $\mathcal{E}$ is the electromotive force (emf).
- N is the number of loops or turns in the coil.
- $\frac{d\Phi}{dt}$ is the rate of change of magnetic flux through the loop.
- L is the inductance of the coil.
- $\frac{di}{dt}$ is the rate of change of current in the coil.

As energy is conserved, this process results in an elevated output voltage, and the voltage gain of a conventional boost converter is given by [6]:

$$V_{out} = \frac{1}{(1-D)}V_{in} \tag{2.2}$$

where D denotes the duty cycle of the switching element. This formulation assumes ideal switching devices and negligible parasitic resistances in the stator windings.

Consequently, a slightly higher duty cycle is required in practice to achieve a doubling of the input voltage.
As illustrated in Figure 2.1, the IPMSM-based booster topology leverages the three-phase stator windings of the machine as the inductive elements of the boost stage. The charging station is connected such that the windings carry the input current, while the inverter bridge legs operate as controlled switching elements (e.g., MOSFETs or diodes, depending on the conduction state).

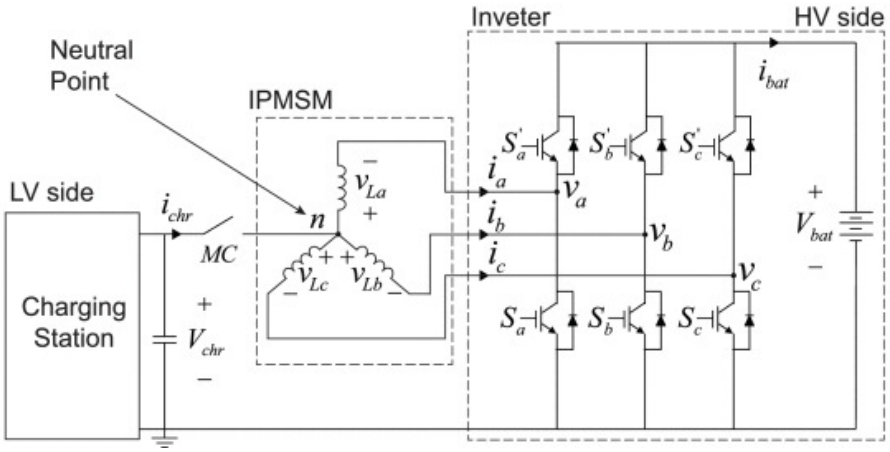

Figure 2.1: The integrated DC-DC booster configuration [1]

2.1.2 IPMSM Saliency and Position-Dependent Inductance

IPMSMs are designed to operate in the relatively low-frequency region 0–1 kHz whereas the charger operating frequency is 10–20 kHz. This results in a large difference in inductance when the IPMSM is used as a motor versus the charger inductor. To accurately model the behaviour of the IPMSM when utilised as a three-phase coupled inductor, the inductance matrix must account for both the average inductance and the spatial variations caused by the rotor's saliency [1].

2.1.2.1 The Non-Salient (Average) Component

First, we consider the machine as a balanced, non-salient inductor. This component consists of the leakage inductance L_{ls} and the mutual air-gap inductance L_m. In this state, the mutual coupling between phases is constant and symmetrical [1]:

$$L_{abc} = \begin{pmatrix} L_{\mathrm{ls}} + L_m & -\frac{L_m}{2} & -\frac{L_m}{2} \\ -\frac{L_m}{2} & L_{\mathrm{ls}} + L_m & -\frac{L_m}{2} \\ -\frac{L_m}{2} & -\frac{L_m}{2} & L_{\mathrm{ls}} + L_m \end{pmatrix} \tag{2.3}$$

2.1.2.2 The Saliency (Position-Dependent) Component

Because the IPMSM has internal permanent magnets, the reluctance of the magnetic path changes as the rotor angle θ varies. This introduces a saliency component, L_δ, which fluctuates at twice the electrical frequency. This variation is captured in the saliency matrix [1]:

$$L_{rlc}(\theta) = \begin{pmatrix} L_\delta \cos(2p\theta) & \sigma_1 & \sigma_2 \\ \sigma_1 & \sigma_2 & L_\delta \cos(2p\theta) \\ \sigma_2 & L_\delta \cos(2p\theta) & \sigma_1 \end{pmatrix}$$

where (2.4)

$$\sigma_1 = L_\delta \cos\left(\frac{2\pi}{3} - 2p\theta\right)$$
$$\sigma_2 = L_\delta \cos\left(\frac{2\pi}{3} + 2p\theta\right)$$

2.1.2.3 The Combined IPMSM Inductance Matrix

By superimposing the average and saliency components ($L_{abc} = L_{\text{avg}} + L_{\text{sal}}$), we arrive at the full inductance matrix used in the state-space model. This matrix defines how the magnetic coupling between phases changes dynamically with the rotor position [1]:

$$L_{abc}(\theta) = \begin{pmatrix} \lambda_1 & \sigma_1 & \sigma_2 \\ \sigma_1 & \lambda_2 & \sigma_3 \\ \sigma_2 & \sigma_3 & \lambda_3 \end{pmatrix}$$

where

$$\begin{aligned} \lambda_1 &= L_{\text{ls}} + L_m - L_\delta \cos(2p\theta) \\ \lambda_2 &= L_{\text{ls}} + L_m - L_\delta \cos\left(\frac{2\pi}{3} + 2p\theta\right) \\ \lambda_3 &= L_{\text{ls}} + L_m - L_\delta \cos\left(\frac{2\pi}{3} - 2p\theta\right) \\ \sigma_1 &= -\frac{L_m}{2} - L_\delta \cos\left(\frac{2\pi}{3} - 2p\theta\right) \\ \sigma_2 &= -\frac{L_m}{2} - L_\delta \cos\left(\frac{2\pi}{3} + 2p\theta\right) \\ \sigma_3 &= -\frac{L_m}{2} - L_\delta \cos(2p\theta) \end{aligned} \tag{2.5}$$

2.1.3 LC Resonant Dynamics

The interaction between the charging station cable impedance, the stator winding network, and the input smoothing capacitor (C) forms an underdamped LC tank circuit, as illustrated in Figure 2.1. When an open-loop step change in duty cycle is applied, this underdamped system gives rise to pronounced oscillations in both the phase currents and the input voltage.
The natural frequency of the resonant network is determined by [6]:

$$f_0 = \frac{1}{2\pi\sqrt{L_s C}} \tag{2.6}$$

2.1.4 Stator-Rotor Field Interactions & Parasitic Torque

Injecting DC charging currents into the AC stator windings generates a stationary stator magnetic field vector. If this field vector is misaligned with the permanent magnet flux vector of the rotor, an unintended electromagnetic torque is produced [5]. The electromagnetic torque of an IPMSM in the synchronous dq frame is given by [2]:

$$T_e = \frac{3}{2} p \left(\psi_m i_q + (L_d - L_q) i_d i_q \right) \tag{2.7}$$

where i_q is the torque-producing current component obtained by projecting the three-phase currents into the rotating reference, see Figure 2.2, using the park-clarke [2]:

$$\begin{bmatrix} i_d \\ i_q \end{bmatrix} = \frac{2}{3} \begin{bmatrix} \cos(\theta) & \cos\left(\theta - \frac{2\pi}{3}\right) & \cos\left(\theta + \frac{2\pi}{3}\right) \\ -\sin(\theta) & -\sin\left(\theta - \frac{2\pi}{3}\right) & -\sin\left(\theta + \frac{2\pi}{3}\right) \end{bmatrix} \begin{bmatrix} i_a \\ i_b \\ i_c \end{bmatrix} \tag{2.8}$$

From the second row of the transformation, the q-axis current can be explicitly written as:

$$i_q = \frac{2}{3} (-\sin(\theta)\, i_a - \sin\left(\theta - \frac{2\pi}{3}\right) i_b - \sin\left(\theta + \frac{2\pi}{3}\right) i_c) \tag{2.9}$$

Under three-phase symmetry, if the phase currents are balanced in their average values,

$$\overline{i_a} = \overline{i_b} = \overline{i_c} \tag{2.10}$$

the fundamental spatial component of the stator current cancels in the synchronous reference frame, resulting in

$$\overline{i_q} = 0 \tag{2.11}$$

In this case, no steady-state torque is produced [1].

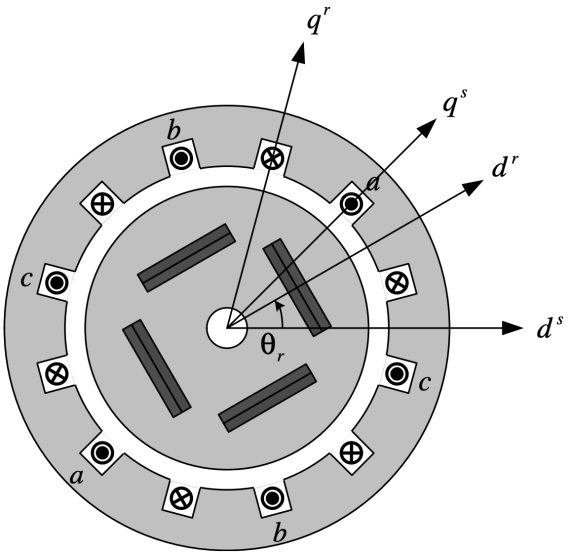

Figure 2.2: Four-pole interior PMSM in the dq frame [2].

2.2 Mathematical Modelling and Linearisation Framework

2.2.1 State-Space Averaged Modelling Principles

The modelling approach is based on two fundamental circuit laws: Kirchhoff's Voltage Law (KVL) and Kirchhoff's Current Law (KCL). KVL states that the algebraic sum of voltages around any closed loop is zero, whilst KCL states that the algebraic sum of currents entering a node must equal the sum of currents leaving that node. These principles remain valid in both switching states of the converter. For a boost converter operating in continuous conduction mode (CCM), two distinct switching intervals are considered: the ON-state and the OFF-state. In each interval, the system dynamics are described by different sets of differential equations derived directly from KVL and KCL [8, 6].

2.2.1.1 ON-State Operation (Switch Closed)

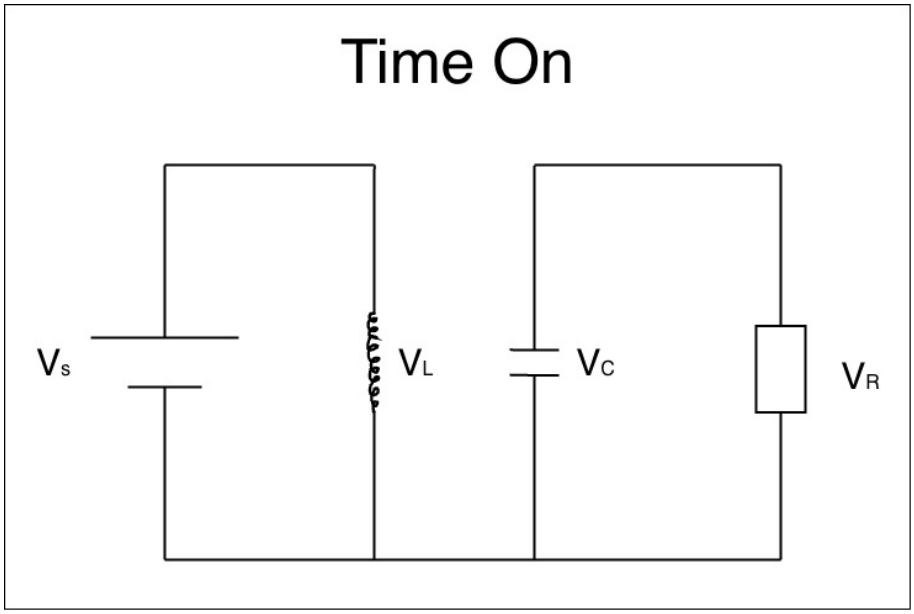

Figure 2.3: Boost converter during the ON-state.

When the switch is closed, the inductor is connected directly to the input voltage source and stores energy in its magnetic field, see Figure 2.3. Applying Kirchhoff's Voltage Law (KVL) around the input loop gives [8, 6]:

$$V_S = V_{in}, \quad V_R = V_{out} \tag{2.12}$$

$$V_L = V_{\text{in}} = L\frac{dI_L}{dt}. \tag{2.13}$$

$$\frac{dI_L}{dt} = \frac{V_{\text{in}}}{L}. \tag{2.14}$$

Equation 2.14 shows that the inductor current increases linearly during the ON-state. At the same time, the diode is reverse-biased, preventing current from flowing to the output stage. The load is therefore supplied solely by the output capacitor. Applying Kirchhoff's Current Law (KCL) at the output node gives [8, 6]:

$$I_C = -I_{\text{out}}, \tag{2.15}$$

$$C\frac{dV_{out}}{dt} = -\frac{V_{out}}{R}. \tag{2.16}$$

$$\frac{dV_{out}}{dt} = -\frac{V_{out}}{RC}. \tag{2.17}$$

2.2.1.2 OFF-State Operation (Switch Open)

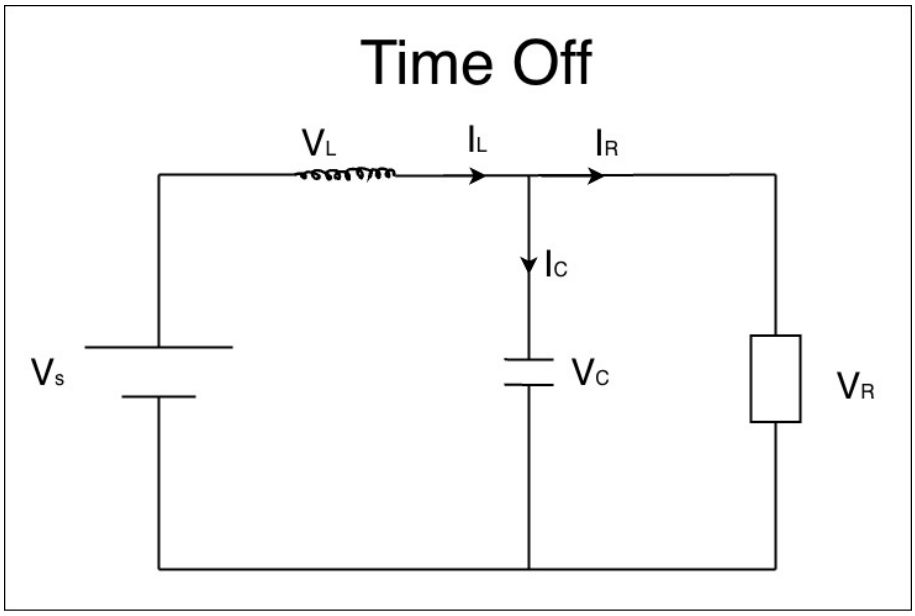

Figure 2.4: Boost converter during the OFF-state.

When the switch is opened, the energy stored in the inductor is transferred to the output through the diode, see Figure 2.4. Applying KVL around the circuit loop gives [8, 6]:

$$V_S = V_{in}, \quad V_R = V_{out} \tag{2.18}$$

$$V_{\text{in}} - L\frac{dI_L}{dt} - V_{out} = 0. \tag{2.19}$$

$$\frac{dI_L}{dt} = \frac{V_{\text{in}} - V_{out}}{L}. \tag{2.20}$$

Applying KCL at the output node shows that the inductor current is divided between the load and the capacitor [8, 6]:

$$I_L = I_R + I_C. \tag{2.21}$$

$$C\frac{dV_{out}}{dt} = I_L - \frac{V_{out}}{R}. \tag{2.22}$$

$$\frac{dV_{out}}{dt} = \frac{I_L}{C} - \frac{V_{out}}{RC}. \tag{2.23}$$

2.2.1.3 State Space Averaging

Let $D \in [0, 1]$ denote the duty cycle, defined as the fraction of the switching period for which the converter is in the ON-state. The averaged state-space model is then obtained by weighting the ON and OFF dynamics [9, 8, 6]:

$$\dot{\mathbf{x}} = D\,\dot{\mathbf{x}}_{\text{on}} + (1-D)\,\dot{\mathbf{x}}_{\text{off}}. \tag{2.24}$$

With the state vector defined as $\mathbf{x} = [i_L \;\; V_{out}]^T$, the averaged boost converter model becomes:

$$\frac{di_L}{dt} = \frac{V_{\text{in}}}{L} - (1-D)\frac{V_{out}}{L}, \tag{2.25}$$

$$\frac{dV_{out}}{dt} = \frac{(1-D)i_L}{C} - \frac{V_{out}}{RC}. \tag{2.26}$$

2.2.2 Multi-Variable Jacobian Linearisation (Taylor Series)

Nonlinear systems can be controlled using a local linear approximation of their dynamics. A continuous nonlinear system can be described in state-space form as [10]:

$$\dot{\mathbf{x}}(t) = \mathbf{f}(\mathbf{x}(t), \mathbf{u}(t)) \tag{2.27}$$

Where $\mathbf{x}(t)$ is the state vector and $\mathbf{u}(t)$ is the input vector.
To linearise this around a specific nominal operating point $(\mathbf{x}_0, \mathbf{u}_0)$, a first-order Taylor series expansion can be used [11, 10]. We assume small perturbations ($\boldsymbol{\Delta}\mathbf{x}$, $\boldsymbol{\Delta}\mathbf{u}$) around this point:

$$\mathbf{x} = \mathbf{x}_0 + \boldsymbol{\Delta}\mathbf{x} \tag{2.28}$$

$$\mathbf{u} = \mathbf{u}_0 + \boldsymbol{\Delta}\mathbf{u} \tag{2.29}$$

Substituting these into the original function gives:

$$\dot{\mathbf{x}}_0 + \dot{\boldsymbol{\Delta}}\mathbf{x} = \mathbf{f}(\mathbf{x}_0 + \boldsymbol{\Delta}\mathbf{x}, \mathbf{u}_0 + \boldsymbol{\Delta}\mathbf{u}) \tag{2.30}$$

Expanding using Taylor series and ignoring Higher-Order Terms (H.O.T.) yields [12]:

$$\dot{\boldsymbol{\Delta}}\mathbf{x} \approx \left.\frac{\partial \mathbf{f}}{\partial \mathbf{x}}\right|_{(\mathbf{x}_0,\mathbf{u}_0)} \boldsymbol{\Delta}\mathbf{x} + \left.\frac{\partial \mathbf{f}}{\partial \mathbf{u}}\right|_{(\mathbf{x}_0,\mathbf{u}_0)} \boldsymbol{\Delta}\mathbf{u} \tag{2.31}$$

This can be rewritten in standard linear state-space form using Jacobian matrices:

$$\dot{\boldsymbol{\Delta}}\mathbf{x} = \mathbf{A}\boldsymbol{\Delta}\mathbf{x} + \mathbf{B}\boldsymbol{\Delta}\mathbf{u} \tag{2.32}$$

Where the system Jacobian matrices $\mathbf{A}$ and $\mathbf{B}$ are defined as:

$$\mathbf{A} = \left.\frac{\partial \mathbf{f}}{\partial \mathbf{x}}\right|_{(\mathbf{x}_0,\mathbf{u}_0)} = \begin{bmatrix} \frac{\partial f_1}{\partial x_1} & \frac{\partial f_1}{\partial x_2} & \cdots & \frac{\partial f_1}{\partial x_n} \\ \frac{\partial f_2}{\partial x_1} & \frac{\partial f_2}{\partial x_2} & \cdots & \frac{\partial f_2}{\partial x_n} \\ \vdots & \vdots & \ddots & \vdots \\ \frac{\partial f_n}{\partial x_1} & \frac{\partial f_n}{\partial x_2} & \cdots & \frac{\partial f_n}{\partial x_n} \end{bmatrix} \tag{2.33}$$

$$\mathbf{B} = \left.\frac{\partial \mathbf{f}}{\partial \mathbf{u}}\right|_{(\mathbf{x}_0,\mathbf{u}_0)} = \begin{bmatrix} \frac{\partial f_1}{\partial u_1} & \frac{\partial f_1}{\partial u_2} & \cdots & \frac{\partial f_1}{\partial u_m} \\ \frac{\partial f_2}{\partial u_1} & \frac{\partial f_2}{\partial u_2} & \cdots & \frac{\partial f_2}{\partial u_m} \\ \vdots & \vdots & \ddots & \vdots \\ \frac{\partial f_n}{\partial u_1} & \frac{\partial f_n}{\partial u_2} & \cdots & \frac{\partial f_n}{\partial u_m} \end{bmatrix} \tag{2.34}$$

2.2.3 Transfer Function Representation of MIMO State-Space Systems

A linear time-invariant continuous-time system in state-space form is given by:

$$\dot{\mathbf{x}} = \mathbf{A}\mathbf{x} + \mathbf{B}\mathbf{u}, \quad \mathbf{y} = \mathbf{C}\mathbf{x} + \mathbf{D}\mathbf{u}. \tag{2.35}$$

The corresponding input–output relation in the Laplace domain is expressed by the transfer function matrix [13]:

$$\mathbf{G}(s) = \mathbf{C}(s\mathbf{I} - \mathbf{A})^{-1}\mathbf{B} + \mathbf{D}. \tag{2.36}$$

For multi-phase systems, the model is inherently MIMO due to multiple duty-cycle inputs and multiple electrical outputs. In the special case where all duty-cycle inputs are constrained to be identical, the system reduces to an equivalent single-input representation, allowing a scalar transfer function description between the common input and selected outputs.

2.3 Advanced Control

2.3.1 Cascaded Architecture and Time-Scale Separation

An integrated booster demands simultaneous regulation of fast electrical current dynamics and slower energy-storage voltage dynamics [4]. Attempting to control this within a single combined loop leads to structural interactions.
By applying successive loop closure, the architecture is split into a fast inner MIMO current loop and a slow outer SISO voltage loop. This hierarchy relies on time-scale separation: the inner current loop operates at a high bandwidth (1kHz), allowing the outer voltage loop (0.1 kHz) to view the entire inner loop as a instantaneous, unity-gain actuator.

2.3.2 State-Space Integral Augmentation

To enforce perfect setpoint tracking and eliminate steady-state errors introduced by parasitic resistance (r_s) or station current fluctuations, tracking integrators must be embedded into the state-space structure. The system is augmented with an error integrator state $\dot{\mathbf{z}} = \mathbf{r} - \mathbf{y}$, yielding the classic augmented state-space format [14, 10]:

$$\begin{bmatrix} \dot{\mathbf{x}} \\ \dot{\mathbf{z}} \end{bmatrix} = \begin{bmatrix} \mathbf{A} & \mathbf{0} \\ -\mathbf{C} & \mathbf{0} \end{bmatrix} \begin{bmatrix} \mathbf{x} \\ \mathbf{z} \end{bmatrix} + \begin{bmatrix} \mathbf{B} \\ \mathbf{0} \end{bmatrix} \mathbf{u} \tag{2.37}$$

2.3.3 Controllability and Observability

2.3.3.1 Controllability

Reachability (controllability) refers to the extent to which the state of a linear control system may be steered through the application of suitable control inputs [10, 15]. Consider the linear state-space system

$$\dot{\mathbf{x}} = \mathbf{A}\mathbf{x} + \mathbf{B}\mathbf{u} \tag{2.38}$$

where $\mathbf{A} \in ..\mathbb{R}^{n\times n}$ is the system matrix and $\mathbf{B} \in \mathbb{R}^{n\times m}$ is the input matrix. The principal question is whether an arbitrary final state $\mathbf{x}_f \in \mathbb{R}^n$ may be reached from a given initial state $\mathbf{x}_0$ within a finite time interval through an appropriate choice of control input $\mathbf{u}(t)$.
The reachability properties of the system are characterised by the reachability matrix [10, 15]:

$$\mathbf{W}_r = \begin{bmatrix} \mathbf{B} & \mathbf{AB} & \mathbf{A}^2\mathbf{B} & \cdots & \mathbf{A}^{n-1}\mathbf{B} \end{bmatrix} \tag{2.39}$$

A linear system is said to be reachable if and only if the matrix $\mathbf{W}_r$ has full rank. Meaning that the rank of $\mathbf{W}_r$ is equal to the number of system states, such that every state can be independently influenced by the control input [10, 15]. This condition implies that the control input generates a sufficient number of linearly independent directions in the state space, thereby enabling arbitrary state transitions. Reachability is therefore a fundamental concept in modern control theory, as it determines the extent to which feedback may be employed to influence or stabilise the dynamics of a system.

2.3.3.2 Observability

Observability theory concerns whether the internal state of a dynamical system may be determined from knowledge of its inputs and measured outputs over a finite interval of time [10, 15]. Consider the linear state-space system:

$$\dot{\mathbf{x}} = \mathbf{Ax} + \mathbf{Bu}, \qquad \mathbf{y} = \mathbf{Cx} + \mathbf{Du} \tag{2.40}$$

where $\mathbf{x} \in \mathbb{R}^n$ denotes the state vector, $\mathbf{u}$ the input, and $\mathbf{y}$ the measured output. A system is said to be observable if the state $\mathbf{x}(t)$ can be uniquely determined from measurements of $\mathbf{u}(t)$ and $\mathbf{y}(t)$.
The observability properties of the system are characterised by the observability matrix [10, 15]:

$$\mathbf{W_o} = \begin{bmatrix} \mathbf{C} \\ \mathbf{CA} \\ \mathbf{CA}^2 \\ \vdots \\ \mathbf{CA}^{n-1} \end{bmatrix} \tag{2.41}$$

A linear system is observable if and only if the matrix $\mathbf{W}_o$ has full rank [10, 15]. This condition ensures that the measured outputs contain sufficient information to reconstruct the internal state of the system. Observability is therefore fundamental in control theory, particularly in the design of state observers and estimation algorithms, where unmeasured states must be inferred from available sensor data.

2.3.4 Stability of Feedback Systems

2.3.4.1 Eigenvalues and Stability

The stability of a linear dynamical system is fundamentally determined by the eigenvalues of its system matrix [10]. Consider the autonomous system:

$$\frac{d\mathbf{x}}{dt} = \mathbf{A}\mathbf{x} \tag{2.42}$$

where $\mathbf{A} \in \mathbb{R}^{n\times n}$. The eigenvalues λ of $\mathbf{A}$ are defined by the characteristic equation:

$$\mathbf{A}\mathbf{v} = \lambda\mathbf{v} \tag{2.43}$$

where $\mathbf{v} \neq 0$ is an eigenvector.
The eigenvalues may be computed from the matrix $\mathbf{A}$ using the spectral decomposition:

$$\mathbf{V} = \begin{bmatrix}\mathbf{v}_1 & \mathbf{v}_2 & \mathbf{v}_3 & \cdots & \mathbf{v}_n\end{bmatrix} \tag{2.44}$$

$$\mathbf{A} = \mathbf{V}\mathbf{D}\mathbf{V}^{-1} \tag{2.45}$$

where $\mathbf{D} = \mathrm{diag}(\lambda_1, \lambda_2, \ldots, \lambda_n)$ contains the eigenvalues on its diagonal.
The stability of the system is determined by the real parts of the eigenvalues. In particular, the system is asymptotically stable if all eigenvalues satisfy [10]:

$$\Re(\lambda_i) < 0 \quad \forall i \tag{2.46}$$

This condition implies that all modes of the system decay exponentially to zero as time progresses. If any eigenvalue has a positive real part, the corresponding mode grows unbounded, and the system is unstable. Eigenvalues with zero real part indicate marginal behaviour, which requires further analysis of the system structure. Hence, eigenvalue analysis provides a direct and fundamental criterion for assessing the stability of linear systems.

2.3.4.2 Bode Stability Margins

Bode stability margins provide a frequency-domain measure of the relative stability and robustness of a feedback control system. The analysis is based on the open-loop transfer function $G(s)$, whose magnitude and phase responses are evaluated using the Bode diagram.
Two principal quantities are used in stability assessment: the gain margin and the phase margin. The gain margin represents the permissible increase in loop gain before the closed-loop system becomes unstable, measured at the phase crossover frequency where the phase reaches $-180°$. The phase margin represents the additional phase lag required to bring the system to the verge of instability at the gain crossover frequency [16], where the magnitude satisfies:

$$|G(j\omega)| = 1 \tag{2.47}$$

The phase margin is therefore defined relative to the critical phase condition:

$$\angle G(j\omega_{cp}) = -180° + \mathrm{PM} \tag{2.48}$$

where ω_{cp} denotes the gain crossover frequency.
Positive gain and phase margins indicate a stable and robust closed-loop system, whereas small or negative margins imply poor robustness and potential instability [17]. In practical control design, phase margins between approximately 30° and 60° are commonly regarded as providing an appropriate compromise between stability and dynamic performance.

2.3.5 Optimal Control via LQR & Bryson's Tuning Rule

The Linear Quadratic Regulator (LQR) is a convex optimisation-based control method that minimises a quadratic cost function for a linear dynamical system, accounting for both state deviation and control effort. [10]

$$\dot{\mathbf{x}} = \mathbf{A}\mathbf{x} + \mathbf{B}\mathbf{u} \tag{2.49}$$

Given a linear dynamical system of the form above, the objective is to minimise the cost function:

$$\begin{aligned} \min_{\mathbf{u}} \quad & J = \int_0^\infty \left(\mathbf{x}^T\mathbf{Q}\mathbf{x} + \mathbf{u}^T\mathbf{R}\mathbf{u}\right) dt \\ \text{subject to} \quad & \dot{\mathbf{x}} = \mathbf{A}\mathbf{x} + \mathbf{B}\mathbf{u} \end{aligned} \tag{2.50}$$

where $\mathbf{Q} \succeq 0$ penalises deviations in the system states and $\mathbf{R} \succ 0$ penalises the control input.
Bryson's rule provides a practical method for selecting the weighting matrices in the cost function [18]. It is defined as:

$$Q_{ii} = \frac{1}{(\max |x_i|_{\text{acceptable}})^2}, \qquad i \in \{1, 2, \ldots, n\} \tag{2.51}$$

$$R_{jj} = \frac{1}{(\max |u_j|_{\text{acceptable}})^2}, \qquad j \in \{1, 2, \ldots, m\} \tag{2.52}$$

The resulting weighting matrices take diagonal form:

$$\mathbf{Q} = \begin{bmatrix} Q_{1,1} & 0 & \cdots & 0 \\ 0 & Q_{2,2} & \cdots & 0 \\ \vdots & \vdots & \ddots & \vdots \\ 0 & 0 & \cdots & Q_{n,n} \end{bmatrix}, \quad \mathbf{R} = \begin{bmatrix} R_{1,1} & 0 & \cdots & 0 \\ 0 & R_{2,2} & \cdots & 0 \\ \vdots & \vdots & \ddots & \vdots \\ 0 & 0 & \cdots & R_{m,m} \end{bmatrix} \tag{2.53}$$

The optimal state-feedback gain is obtained by solving the continuous-time algebraic Riccati equation:

$$\mathbf{A}^T\mathbf{P} + \mathbf{P}\mathbf{A} - \mathbf{P}\mathbf{B}\mathbf{R}^{-1}\mathbf{B}^T\mathbf{P} + \mathbf{Q} = 0 \tag{2.54}$$

where $\mathbf{P}$ is a positive definite matrix representing the optimal cost-to-go. The resulting optimal feedback gain is then given by:

$$\mathbf{K} = \mathbf{R}^{-1}\mathbf{B}^T\mathbf{P} \tag{2.55}$$

$$\mathbf{u} = -\mathbf{K}\mathbf{x} \tag{2.56}$$

2.3.6 Pole Placement

Pole placement is a state-feedback control technique used to assign the closed-loop poles of a linear system to desired locations in the complex plane. The pole locations directly determine key system properties such as stability, settling time, and damping [19].
Consider the linear system:

$$\dot{\mathbf{x}} = \mathbf{A}\mathbf{x} + \mathbf{B}\mathbf{u} \tag{2.57}$$

A state-feedback controller is defined as:

$$\mathbf{u} = -\mathbf{K}\mathbf{x} \tag{2.58}$$

which yields the closed-loop system:

$$\dot{\mathbf{x}} = (\mathbf{A} - \mathbf{B}\mathbf{K})\mathbf{x} \tag{2.59}$$

The objective is to choose $\mathbf{K}$ such that the eigenvalues of $(\mathbf{A} - \mathbf{B}\mathbf{K})$ are placed at desired locations, shaping the transient response of the system.
Pole placement is only possible if the system $(\mathbf{A}, \mathbf{B})$ is controllable, and poor pole choices (e.g., too far left in the complex plane) can lead to high control effort and sensitivity to disturbances. Modern algorithms, such as the robust pole assignment method by Kautsky, Nichols, and Van Dooren, improve numerical stability and exploit multi-input freedom to obtain more reliable solutions [20].

2.3.7 Large-Signal Disturbance Feedforward Design

Unlike feedback control, which reacts only after a disturbance has affected the system, feedforward control acts proactively by using a plant model or direct disturbance measurements to determine the required control action in advance. When combined with feedback control, this forms a two-degree-of-freedom (2-DOF) architecture that improves disturbance rejection while maintaining closed-loop robustness.
If a disturbance can be measured before it propagates through the plant, a feedforward compensator can be used to generate a corrective control action that counteracts its effect on the output [21]. For ideal disturbance cancellation, the feedforward compensator is given by:

$$G_{ff}(s) = -\frac{G_d(s)}{G_p(s)}, \tag{2.60}$$

Where $G_d(s)$ represents the disturbance dynamics and $G_p(s)$ the plant dynamics. Since the feedforward path does not alter the closed-loop characteristic equation, it can significantly improve disturbance rejection without compromising system stability.
§

3
Methods

3.1 System Topology

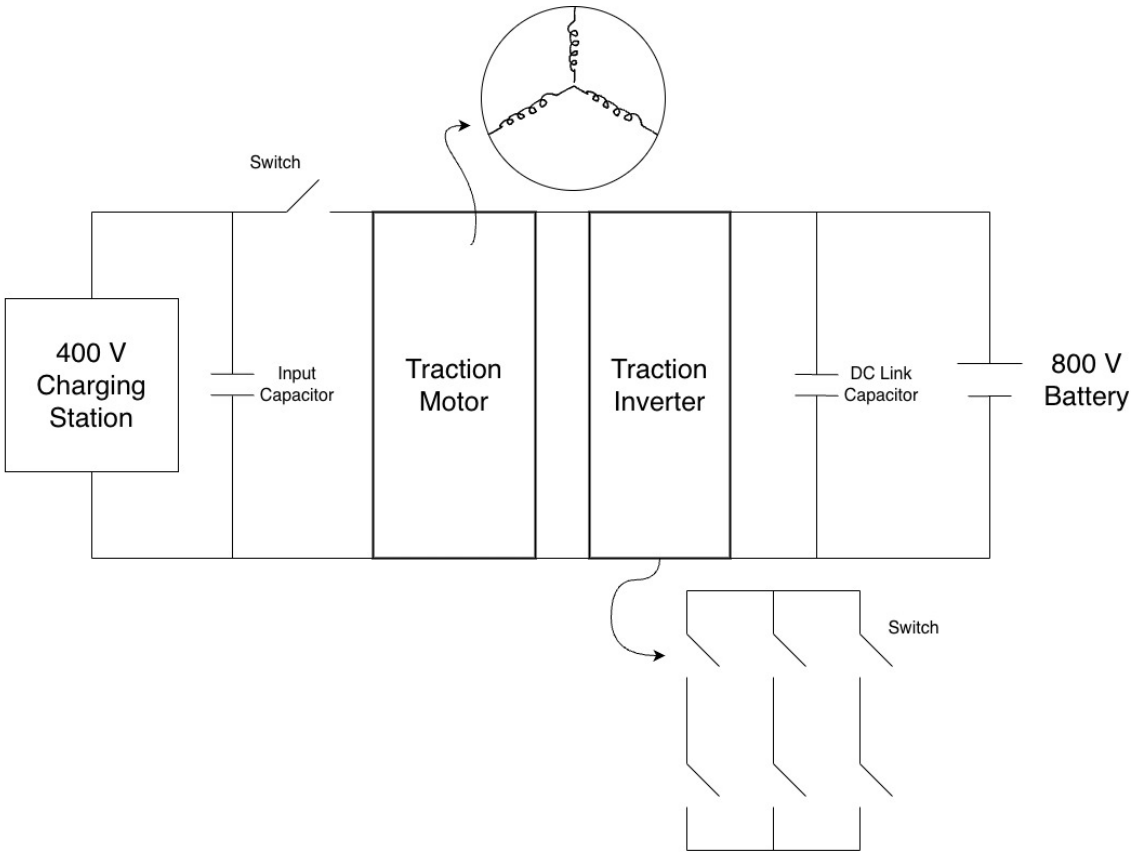

Figure 3.1: Functional block diagram of the DC-coupled charging path from station to high-voltage battery.

Since the charging station voltage is lower than the battery voltage, the system must boost the voltage to supply current to the battery. This is achieved by using the copper windings of the stator of the electrical machine as the inductive element, as shown in Figure 3.1. An input capacitor is placed close to the charging station side, and an output capacitor is placed close to the battery side. Because the EV battery has a high voltage and large energy capacity, the output capacitor exhibits only slow dynamics. The control objective is to boost the input voltage without introducing voltage spikes or damaging transients in the capacitors. At the same

time, the phase currents in the stator windings must be carefully controlled to avoid inducing steady-state torque in the rotor during charging.

3.1.1 Integrated Booster Configuration

The complete system configuration is summarised in Tables 3.1–3.2.

Table 3.1: System parameters used for the integrated boost-converter model.

Parameter	Symbol	Value
Charging station voltage	$V_{station}$	400 V
Battery voltage	$V_{battery}$	800 V
Station current limit	$I_{station}$	300 A
Input capacitor	C_{in}	2 mF
Output capacitor	C_{out}	5 mF
Input cable resistance	R_{in}	20 mΩ
Battery-side resistance	R_{out}	10 mΩ
Switching frequency	f_{sw}	10 kHz
Nominal duty ratio	D	0.5

Table 3.2: Electrical and winding parameters of the IPMSM [1].

Parameter	Value
Mutual inductance (L_m)	125 μH @ 100 Hz 50 μH @ 10 kHz
Leakage inductance (L_{ls})	45 μH @ 100 Hz 75 μH @ 10 kHz
Saliency inductance (L_δ)	30 μH @ 100 Hz 40 μH @ 10 kHz
Coil resistance (r_s)	0.009 Ω
Number of pole pairs (p)	4

3.2 Mathematical Modelling of the IPMSM Booster

The system dynamics are modeled by analysing the energy flow in two distinct states: the On Mode (energy storage) and the Off Mode (energy transfer). We represent the system using the state vector $\mathbf{x}$ and control vector $\mathbf{u}$:

$$\mathbf{x} = \begin{bmatrix} i_a & i_b & i_c & V_{C_{in}} & V_{C_{out}} \end{bmatrix}^T, \quad \mathbf{u} = \begin{bmatrix} D_a & D_b & D_c \end{bmatrix}^T \tag{3.1}$$

3.2.1 Circuit Law Application (On Mode)

In this mode, the low-side switches are closed, grounding the inductor terminals. We apply Kirchhoff's Voltage Law (KVL) to the input loops to determine current

growth and Kirchhoff's Current Law (KCL) to the capacitor nodes to determine voltage fluctuations. The phase inductors act as energy storage elements, charging their magnetic field when the low-side switches are closed. During this "On" interval, the inductors are connected directly between the input capacitor and the negative DC rail. The input capacitor balances the station supply against the phase draw, while the output capacitor independently supports the battery.
Inductor Dynamics (KVL):

$$v_{L_{abc}} = v_{C_{in}} - v_{r_s} \tag{3.2}$$

$$\mathbf{L}_{abc}(\theta)\frac{d\mathbf{i}_{abc}}{dt} = v_{C_{in}} - r_s\mathbf{i}_{abc} \tag{3.3}$$

$$\frac{d\mathbf{i}_{abc}}{dt} = \mathbf{L}_{abc}^{-1}(\theta)\left(\mathbf{v}_{C_{in}} - r_s\mathbf{i}_{abc}\right) \tag{3.4}$$

Input Capacitor Dynamics (KCL):

$$I_{C_{in}} = I_{Station} - \sum_{x\in a,b,c} i_x \tag{3.5}$$

$$C_{in}\frac{dV_{C_{in}}}{dt} = \frac{V_{Station} - V_{C_{in}}}{R_{in}} - \sum_{x\in a,b,c} i_x \tag{3.6}$$

$$\frac{dV_{C_{in}}}{dt} = \frac{1}{C_{in}}\left(\frac{V_{Station} - V_{C_{in}}}{R_{in}} - (i_a + i_b + i_c)\right) \tag{3.7}$$

Output Capacitor Dynamics (KCL):

$$I_{C_{out}} = I_{battery} \tag{3.8}$$

$$C_{out}\frac{dV_{C_{out}}}{dt} = \frac{V_{C_{out}} - V_{Battery}}{R_{out}} \tag{3.9}$$

$$\frac{dV_{C_{out}}}{dt} = \frac{1}{C_{out}}(\frac{V_{C_{out}} - V_{Battery}}{R_{out}}) \tag{3.10}$$

3.2.2 Circuit Law Application (Off Mode)

The dynamics of the input capacitor remain identical to the "On" mode, as the station continues to supply the capacitor while the phases draw current.
Inductor Dynamics (KVL):

$$v_{L_{abc}} = v_{C_{in}} - v_{r_s} - v_{C_{out}} \tag{3.11}$$

$$\mathbf{L}_{abc}(\theta)\frac{d\mathbf{i}_{abc}}{dt} = v_{C_{in}} - v_{C_{out}} - r_s\mathbf{i}_{abc} \tag{3.12}$$

$$\frac{d\mathbf{i}_{abc}}{dt} = \mathbf{L}_{abc}^{-1}(\theta)\left(v_{C_{in}} - v_{C_{out}} - r_s\mathbf{i}_{abc}\right) \tag{3.13}$$

Input Capacitor Dynamics (KCL):

$$\frac{dV_{C_{in}}}{dt} = \frac{1}{C_{in}} \left(\frac{V_{Station} - V_{C_{in}}}{R_{in}} - (i_a + i_b + i_c) \right) \tag{3.14}$$

Output Capacitor Dynamics (KCL):

$$\sum_{x \in \{a,b,c\}} i_x = I_{C_{out}} + I_{Battery} \tag{3.15}$$

$$C_{out} \frac{dV_{C_{out}}}{dt} = \sum_{x \in \{a,b,c\}} i_x - \frac{V_{C_{out}} - V_{Battery}}{R_{out}} \tag{3.16}$$

$$\frac{dV_{C_{out}}}{dt} = \frac{1}{C_{out}} \left((i_a + i_b + i_c) - \frac{V_{C_{out}} - V_{Battery}}{R_{out}} \right) \tag{3.17}$$

3.2.3 The nonlinear space averaged differential equation

To capture the average dynamics between on and off mode is as simple as linear interpolation between the states. This approximation is valid due to the small time frame between on and off mode. We use duty to capture the relation between these two dynamical states.
Our dynamics slightly change if the charging station provides constant voltage or constant current. The formulation for both scenarios is below.
The charging station providing constant voltage:

$$\frac{d\mathbf{i}_{abc}}{dt} = \mathbf{L}_{abc}^{-1}(\theta) \left(v_{C_{in}} - (1 - \mathbf{D}) v_{C_{out}} - r_s \mathbf{i}_{abc} \right) \tag{3.18}$$

$$\frac{dV_{C_{in}}}{dt} = \frac{1}{C_{in}} \left(\frac{V_{Station} - V_{C_{in}}}{R_{in}} - (i_a + i_b + i_c) \right) \tag{3.19}$$

$$\frac{dV_{C_{out}}}{dt} = \frac{1}{C_{out}} \left((1 - \mathbf{D})(i_a + i_b + i_c) - \frac{V_{C_{out}} - V_{Battery}}{R_{out}} \right) \tag{3.20}$$

The charging station provides a constant current:

$$\frac{d\mathbf{i}_{abc}}{dt} = \mathbf{L}_{abc}^{-1}(\theta) \left(v_{C_{in}} - (1 - \mathbf{D}) v_{C_{out}} - r_s \mathbf{i}_{abc} \right) \tag{3.21}$$

$$\frac{dV_{C_{in}}}{dt} = \frac{1}{C_{in}} \left(I_{station} - (i_a + i_b + i_c) \right) \tag{3.22}$$

$$\frac{dV_{C_{out}}}{dt} = \frac{1}{C_{out}} \left((1 - D)(i_a + i_b + i_c) - \frac{V_{C_{out}} - V_{Battery}}{R_{out}} \right) \tag{3.23}$$

3.2.4 The Analytical Inductance Inverse

To accurately model the behaviour of the IPMSM when utilised as a three-phase coupled inductor, the inductance matrix must account for both the average inductance and the spatial variations caused by the rotor's saliency [1].
The state-space model requires the inversion of the position-dependent inductance matrix. The analytical inverse, $\mathbf{L}_{abc}^{-1}(\theta)$, is expressed by isolating the common denominator σ_6 and identifying the symmetrical components as follows:

$$\mathbf{L}_{abc}^{-1}(\theta) = \frac{1}{\sigma_6}\begin{pmatrix}\lambda_1 & \sigma_2 & \sigma_1\\ \sigma_2 & \lambda_2 & \sigma_3\\ \sigma_1 & \sigma_3 & \lambda_3\end{pmatrix}$$

where

$$\begin{aligned}
\lambda_1 &= -3L_\delta^2 + 4\sigma_7 L_\delta L_{\text{ls}} + 4L_{\text{ls}}^2 + 8L_{\text{ls}}L_m + 3L_m^2\\
\lambda_2 &= -3L_\delta^2 - 4\sigma_4 L_\delta L_{\text{ls}} + 4L_{\text{ls}}^2 + 8L_{\text{ls}}L_m + 3L_m^2\\
\lambda_3 &= -3L_\delta^2 - 4\sigma_5 L_\delta L_{\text{ls}} + 4L_{\text{ls}}^2 + 8L_{\text{ls}}L_m + 3L_m^2
\end{aligned} \tag{3.24}$$

$$\begin{aligned}
\sigma_1 &= -3L_\delta^2 - 4L_{\text{ls}}\sigma_5 L_\delta + 3L_m^2 + 2L_{\text{ls}}L_m\\
\sigma_2 &= -3L_\delta^2 - 4L_{\text{ls}}\sigma_4 L_\delta + 3L_m^2 + 2L_{\text{ls}}L_m\\
\sigma_3 &= -3L_\delta^2 + 4L_{\text{ls}}\sigma_7 L_\delta + 3L_m^2 + 2L_{\text{ls}}L_m
\end{aligned}$$

$$\sigma_4 = \cos\left(2p\theta - \tfrac{2\pi}{3}\right), \qquad \sigma_5 = \cos\left(2p\theta + \tfrac{2\pi}{3}\right), \qquad \sigma_7 = \cos(2p\theta)$$

$$\sigma_6 = L_{\text{ls}}\left(-9L_\delta^2 + 4L_{\text{ls}}^2 + 12L_{\text{ls}}L_m + 9L_m^2\right)$$

3.2.5 Phase Shedding

The system behaves differently depending on whether current is applied to one, two, or all three stator windings. The windings act as inductors that increase the voltage, while the stator magnetic field interacts with the rotor's permanent magnetic field, affecting overall dynamics. These changing operating modes are modelled simply by inserting zeros into the inverse inductance matrix and the duty cycle vector, without altering the overall structure. It is important to identify the region with the lowest inductance along the diagonal and avoid placing zeros there. Overestimating inductance can cause controller instability, whereas underestimation is less critical.
3-phase operation:

$$\mathbf{L}_{3ph}^{-1}(\theta) = \frac{1}{\sigma_6}\begin{pmatrix}\lambda_1 & \sigma_2 & \sigma_1\\ \sigma_2 & \lambda_2 & \sigma_3\\ \sigma_1 & \sigma_3 & \lambda_3\end{pmatrix}, \quad \mathbf{D} = [D_a, D_b, D_c]^T \tag{3.25}$$

2-phase operation:

$$\mathbf{L}_{2ph}^{-1}(\theta) = \frac{1}{\sigma_6}\begin{pmatrix}\lambda_1 & \sigma_2 & 0\\ \sigma_2 & \lambda_2 & 0\\ 0 & 0 & 0\end{pmatrix}, \quad \mathbf{D} = [D_a, D_b, 0]^T \tag{3.26}$$

1-phase operation:

$$\mathbf{L}_{1ph}^{-1}(\theta) = \frac{1}{\sigma_6}\begin{pmatrix}\lambda_1 & 0 & 0\\ 0 & 0 & 0\\ 0 & 0 & 0\end{pmatrix}, \quad \mathbf{D} = [D_a, 0, 0]^T \tag{3.27}$$

3.2.6 Linearisation via Jacobian

3.2.6.1 Linearisation

Given that the battery operates at a high voltage and is permanently connected to the output capacitor, the voltage across the output capacitor experiences only negligible variation. The battery effectively suppresses the dynamics of the output capacitor, causing the capacitor voltage to remain close to the battery voltage. Consequently, this side of the system can be considered stiff, allowing the model complexity to be reduced.
Furthermore, most charging stations at which the vehicle is expected to stop provide a controlled constant input current. Under these assumptions, Equations 3.21–3.23 can be simplified to:

$$\frac{d\mathbf{i}_{abc}}{dt} = \mathbf{L}_{abc}^{-1}(\theta)\left(\mathbf{v}_{C_{in}} - (1-D)v_{Battery} - r_s\mathbf{i}_{abc}\right) \tag{3.28}$$

$$\frac{dV_{C_{in}}}{dt} = \frac{1}{C_{in}}\left(I_{station} - (i_a + i_b + i_c)\right) \tag{3.29}$$

The system is characterised by a lack of explicit control authority over the battery's state of charge (SOC) and the constant input current provided by the charging station. Consequently, variables such as $I_{station}$ and $V_{battery}$ must be treated as exogenous inputs, external signals that influence the system but cannot be manipulated by the controller. The system is fundamentally control-affine with a state-dependent input matrix, which introduces nonlinear behaviour. However, a significant coupling exists between the battery voltage and the duty cycle, which renders the system's mapping non-convex. Because of this non-convexity, standard global optimisation techniques are not directly applicable. Instead, the system must be approximated by finding a stationary operating point and performing a local linearisation.
The state-space representation of the system is defined by the state vector $\mathbf{x}$, the control input vector $\mathbf{u}$ and the exogenous disturbance vector $\mathbf{w}$:

$$\mathbf{x} = \begin{bmatrix} i_a & i_b & i_c & V_{C_{in}}\end{bmatrix}^T, \quad \mathbf{u} = \begin{bmatrix} D_a & D_b & D_c\end{bmatrix}^T \mathbf{w} = \begin{bmatrix} I_{station} & V_{battery}\end{bmatrix}^T \tag{3.30}$$

Our system:

$$\dot{\mathbf{x}} = \mathbf{f}(\mathbf{x}, \mathbf{u}, \mathbf{w}) \tag{3.31}$$

$$\dot{\mathbf{x}} = \mathbf{A}\mathbf{x} + \mathbf{B}_\mathbf{u}\mathbf{u} + \mathbf{B}_\mathbf{w}\mathbf{w} \tag{3.32}$$

The system is linearised around an equilibrium point $\bar{\mathbf{x}}$, $\bar{\mathbf{u}}$, $\bar{\mathbf{w}}$ using first order Taylor expansion. To simplify the Taylor expansion, we define an augmented input vector $\bar{\mathbf{z}}$, which encapsulates the states, control authority, and exogenous signals:

$$\mathbf{z} = \begin{bmatrix} \mathbf{x} & \mathbf{u} & \mathbf{w} \end{bmatrix}^T \tag{3.33}$$

$$\mathbf{z} = \bar{\mathbf{z}} + \Delta\mathbf{z} \implies \dot{\mathbf{z}} = \mathbf{f}(\mathbf{z}) = \mathbf{f}(\bar{\mathbf{z}} + \Delta\mathbf{z}) \tag{3.34}$$

$$\mathbf{f}(\mathbf{z}) \approx \underbrace{\mathbf{f}(\bar{\mathbf{z}})}_{0} + \frac{D\mathbf{f}}{D\mathbf{z}}(\bar{\mathbf{z}}) \cdot \Delta\mathbf{z} + \underbrace{\frac{D^2\mathbf{f}}{D\mathbf{z}^2}(\bar{\mathbf{z}}) \cdot \Delta\mathbf{z}^2 + \dots}_{\text{very small}} \tag{3.35}$$

The following derivatives represent the elements of the Jacobian matrix for the state variables i_{abc} and V_{cin}:

$$\frac{\partial \dot{i}_{abc}}{\partial i_{abc}} = -\mathbf{L}^{-1}(\theta) r_s \tag{3.36}$$

$$\frac{\partial \dot{i}_{abc}}{\partial V_{cin}} = \mathbf{L}^{-1}(\theta) \tag{3.37}$$

$$\frac{\partial \dot{i}_{abc}}{\partial D} = -\mathbf{L}^{-1}(\theta) V_{battery} \tag{3.38}$$

$$\frac{\partial \dot{i}_{abc}}{\partial V_s} = 0 \tag{3.39}$$

$$\frac{\partial \dot{i}_{abc}}{\partial V_b} = -\mathbf{L}^{-1}(\theta)(1 - \mathbf{D}) \tag{3.40}$$

$$\frac{\partial \dot{V}_{cin}}{\partial i_{abc}} = -\frac{1}{C_{in}} \tag{3.41}$$

$$\frac{\partial \dot{V}_{cin}}{\partial V_{cin}} = -\frac{1}{C_{in} R_{in}} \tag{3.42}$$

$$\frac{\partial \dot{V}_{cin}}{\partial D} = 0 \tag{3.43}$$

$$\frac{\partial \dot{V}_{cin}}{\partial V_s} = \frac{1}{C_{in} R_{in}} \tag{3.44}$$

$$\frac{\partial \dot{V}_{cin}}{\partial V_b} = 0 \tag{3.45}$$

3.2.6.2 Equilibrium Operating Point

The non-linearity when the rotor is fixed during charging arises from the system inputs, namely the duty cycle and the battery voltage, which act as the control input and disturbance, respectively. To determine a stable operating point that accounts for the internal resistance of the IPMSM, the following approach is used. The battery voltage is chosen to define the equilibrium duty cycle. At equilibrium, the change in average current is zero, giving:

$$\mathbf{L}_{abc}^{-1}(\theta) \left(v_{C_{in}} - (1 - \mathbf{D}) v_{Battery} - r_s \mathbf{i}_{abc} \right) = 0 \tag{3.46}$$

$$v_{C_{in}} - (1 - \mathbf{D}) v_{Battery} - r_s \mathbf{i}_{abc} = 0 \tag{3.47}$$

From this, the equilibrium duty ratios for each phase can be written as:

$$\bar{D}_a = 1 - \frac{v_{C_{in}} - r_s \dot{i}_a}{\bar{V}_b} \tag{3.48}$$

$$\bar{D}_b = 1 - \frac{v_{C_{in}} - r_s \dot{i}_b}{\bar{V}_b} \tag{3.49}$$

$$\bar{D}_c = 1 - \frac{v_{C_{in}} - r_s \dot{i}_c}{\bar{V}_b} \tag{3.50}$$

This shows that the stationary operating point of the linearised state-space model, see Table 3.3, is bounded by the standard boost converter equation.

Table 3.3: Linearisation variables and equilibrium operating point for state-space model

Linearisation variable	**Operating Point**
Duty cycle	$\bar{D} = 0.5$
Battery voltage	$\bar{V}_b = 800\,\mathrm{V}$

3.2.7 The Linearised State-Space Matrices

The linearised system:

$$\Delta\mathbf{x} = \begin{bmatrix}\Delta i_a & \Delta i_b & \Delta i_c & \Delta V_{C_{in}}\end{bmatrix}^T, \quad \Delta\mathbf{u} = \begin{bmatrix}\Delta D_a & \Delta D_b & \Delta D_c\end{bmatrix}^T \tag{3.51}$$

$$\Delta\mathbf{w} = \begin{bmatrix}\Delta I_{station} & \Delta V_{battery}\end{bmatrix}^T \tag{3.52}$$

$$\Delta\dot{\mathbf{x}} = \mathbf{A}\Delta\mathbf{x} + \mathbf{B_u}\Delta\mathbf{u} + \mathbf{B_w}\Delta\mathbf{w} \tag{3.53}$$

$$\Delta\mathbf{y} = \mathbf{C}\Delta\mathbf{x} + \underbrace{\mathbf{D_u}\Delta\mathbf{u}}_{0} + \underbrace{\mathbf{D_w}\Delta\mathbf{w}}_{0} \tag{3.54}$$

The state matrix $\mathbf{A}$ and the control input matrix $\mathbf{B_u}$ are defined as:

$$\mathbf{A} = \begin{bmatrix} -L_{11}^{-1}r_s & -L_{12}^{-1}r_s & -L_{13}^{-1}r_s & L_a^{-1} \\ -L_{21}^{-1}r_s & -L_{22}^{-1}r_s & -L_{23}^{-1}r_s & L_b^{-1} \\ -L_{31}^{-1}r_s & -L_{32}^{-1}r_s & -L_{33}^{-1}r_s & L_c^{-1} \\ -\frac{1}{C_{in}} & -\frac{1}{C_{in}} & -\frac{1}{C_{in}} & 0 \end{bmatrix}, \quad \mathbf{B_u} = \begin{bmatrix} L_{11}^{-1}\bar{V}_b & L_{12}^{-1}\bar{V}_b & L_{13}^{-1}\bar{V}_b \\ L_{21}^{-1}\bar{V}_b & L_{22}^{-1}\bar{V}_b & L_{23}^{-1}\bar{V}_b \\ L_{31}^{-1}\bar{V}_b & L_{32}^{-1}\bar{V}_b & L_{33}^{-1}\bar{V}_b \\ 0 & 0 & 0 \end{bmatrix} \tag{3.55}$$

The disturbance matrix $\mathbf{B_w}$ and output matrix $\mathbf{C}$ are given by:

$$\mathbf{B_w} = \begin{bmatrix} 0 & L_a^{-1}(\bar{d}-1) \\ 0 & L_b^{-1}(\bar{d}-1) \\ 0 & L_c^{-1}(\bar{d}-1) \\ \frac{1}{C_{in}} & 0 \end{bmatrix}, \quad \mathbf{C} = \begin{bmatrix} 1 & 0 & 0 & 0 \\ 0 & 1 & 0 & 0 \\ 0 & 0 & 1 & 0 \\ 0 & 0 & 0 & 1 \end{bmatrix} \tag{3.56}$$

$$L_a^{-1} = L_{11}^{-1} + L_{12}^{-1} + L_{13}^{-1} \tag{3.57}$$

$$L_b^{-1} = L_{21}^{-1} + L_{22}^{-1} + L_{23}^{-1} \tag{3.58}$$

$$L_c^{-1} = L_{31}^{-1} + L_{32}^{-1} + L_{33}^{-1} \tag{3.59}$$

$$\begin{bmatrix} L_{11}^{-1} & L_{12}^{-1} & L_{13}^{-1} \\ L_{21}^{-1} & L_{22}^{-1} & L_{23}^{-1} \\ L_{31}^{-1} & L_{32}^{-1} & L_{33}^{-1} \end{bmatrix} = \mathbf{L}_{abc}^{-1}(\theta) \tag{3.60}$$

3.2.8 Sensor Reduction and Measurement Improvement

An observability analysis of the MIMO system shows that only two current sensors are required to achieve full state feedback control. The remaining states, namely the output voltage and the third current, can be estimated using a state observer. However, due to the fast switching dynamics of the system, a state estimation technique such as a Kalman filter would need to operate at a sampling rate significantly faster than that of the fastest inner current control loop. Achieving such computational performance is generally not feasible with practical hardware implementations.
Furthermore, reducing the bandwidth of the cascade control architecture to accommodate a slower state estimator would not be desirable. The controller must be able to react rapidly to disturbances in order to suppress voltage spikes and protect the hardware from potentially damaging operating conditions. For this reason, although the system is fully observable with only two current measurements, see Equation 3.61–3.63, retaining direct measurements of the critical states provides a more practical and robust solution.

$$\mathbf{C}_r = \begin{bmatrix} 1 & 0 & 0 & 0 \\ 0 & 1 & 0 & 0 \end{bmatrix} \tag{3.61}$$

The observability matrix is then defined as:

$$\mathbf{W_o} = \begin{bmatrix} \mathbf{C}_r \\ \mathbf{C}_r\mathbf{A} \\ \mathbf{C}_r\mathbf{A}^2 \\ \mathbf{C}_r\mathbf{A}^3 \end{bmatrix} \tag{3.62}$$

Evaluation of the observability matrix using MATLAB's `rank()` function gives:

$$\text{rank}(\mathbf{W}_o) = 4. \tag{3.63}$$

Since the rank of the observability matrix is equal to the number of system states, the reduced measurement configuration preserves full observability of the system. Therefore, all states can, in principle, be reconstructed from the two measured currents. However, for the reasons discussed previously, it is preferable to retain direct measurements of all four states rather than rely on state estimation alone.

3.2.9 Transferfunction of the linearised system

The transfer function (TF) is employed to verify the accuracy of the state-space model against an independent circuit model. Under an identical duty cycle input, both models should ideally yield the exact same voltage or current output. Because a transfer function specifically maps a signal input to a signal output, a uniform duty cycle is applied across all phases to observe and evaluate the resulting output state.
To align with this single-input framework, the B matrix is manipulated so that it represents a single signal input.

$$G(s) = \mathbf{C}inv(s\mathbf{I} - \mathbf{A})\mathbf{B} \tag{3.64}$$

Assuming balanced three-phase operation, identical duty cycles, negligible saliency variation around the operating point, and symmetric current sharing, the coupled inductance matrix may be approximated by an equivalent scalar inductance L_{ls}, yielding the following reduced-order SISO transfer function.

$$G_{V_{\text{cin}}}(s) = -\frac{3\, v_{\text{battery},e}}{C_{\text{in}}\, L_{\text{ls}}\, s^2 + C_{\text{in}}\, r_s\, s + 3} \tag{3.65}$$

$$G_{I_{\text{a}}}(s) = \frac{C_{\text{in}}\, s\, v_{\text{battery},e}}{C_{\text{in}}\, L_{\text{ls}}\, s^2 + C_{\text{in}}\, r_s\, s + 3} \tag{3.66}$$

$$G_{I_{\text{b}}}(s) = \frac{C_{\text{in}}\, s\, v_{\text{battery},e}}{C_{\text{in}}\, L_{\text{ls}}\, s^2 + C_{\text{in}}\, r_s\, s + 3} \tag{3.67}$$

$$G_{I_{\text{c}}}(s) = \frac{C_{\text{in}}\, s\, v_{\text{battery},e}}{C_{\text{in}}\, L_{\text{ls}}\, s^2 + C_{\text{in}}\, r_s\, s + 3} \tag{3.68}$$

3.3 Cascade Control Architecture

3.3.1 The cascaded architecture

The 4-state linearised model derived in Section 3.2.7 provides a complete representation of the system dynamics. However, when integral action is introduced through state-space augmentation, the system expands into a single (8 x 8) model consisting of four physical states and four integral states. Attempting to directly control this fully augmented system reveals a significant limitation: rank deficiency.

This limitation arises because the input capacitor voltage ($V_{C_{in}}$) is physically dependent on the sum of the phase currents. As a result, the system does not possess sufficient independent control authority to simultaneously regulate all augmented states within a single-loop control structure. Consequently, the fully augmented system cannot satisfy all integral constraints while maintaining full controllability.

To overcome this issue and retain integral action for eliminating steady-state error, the control structure is decoupled into a cascaded architecture based on time-scale separation. In this configuration, two dependent controllers are implemented: a fast inner-loop (6 x 6) MIMO current controller and a slower outer-loop (2 x 2) voltage controller, see Figure 3.2.

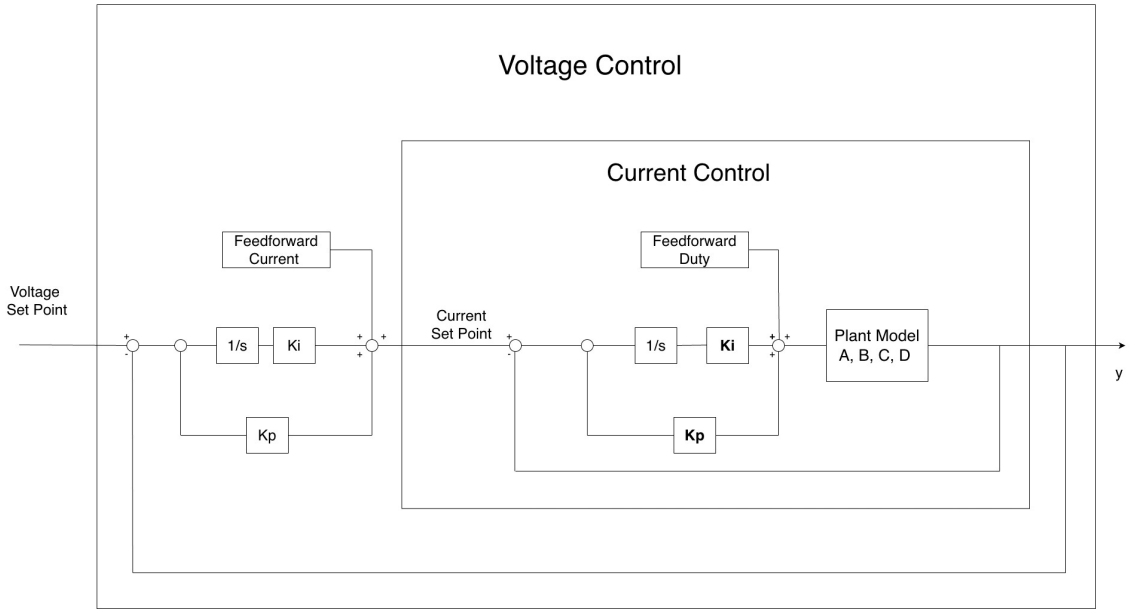

Figure 3.2: Cascade Control Architecture

3.3.2 State-Space Integral Action

To achieve zero steady-state error for the phase currents and input voltage, the state vector is augmented with the integral of the tracking error:

$$\dot{\mathbf{z}}(t) = \mathbf{r}(t) - \mathbf{y}(t) = \mathbf{r}(t) - \mathbf{C}_{track}x(t) \tag{3.69}$$

Where $\dot{\mathbf{z}}(t)$ is the derivative of our integral state, given that each of our states will have integral action we therefore get a doubling in states and subsequently a larger new A and B matrix. The resulting augmented system is defined as:

$$\begin{bmatrix}\dot{\mathbf{x}}\\ \dot{\mathbf{z}}\end{bmatrix} = \begin{bmatrix}\mathbf{A} & 0\\ -\mathbf{C}_{track} & 0\end{bmatrix}\begin{bmatrix}\mathbf{x}\\ \mathbf{z}\end{bmatrix} + \begin{bmatrix}\mathbf{B}\\ 0\end{bmatrix}\mathbf{u} \tag{3.70}$$

3.3.3 Inner-Loop MIMO Current Control

3.3.3.1 System Formulation, Matrix Decoupling, and Integral Augmentation

The inner control loop governs the high-frequency current dynamics of the system. To facilitate the controller synthesis, the coupled three-phase current dynamics are isolated from system matrix equation 3.55 and represented in state-space form as:

$$\Delta\mathbf{x} = \begin{bmatrix}\Delta i_a & \Delta i_b & \Delta i_c\end{bmatrix}^T, \qquad \Delta\mathbf{u} = \begin{bmatrix}\Delta D_a & \Delta D_b & \Delta D_c\end{bmatrix}^T. \tag{3.71}$$

The corresponding linearised dynamics are expressed as:

$$\Delta\dot{\mathbf{x}} = \mathbf{A_i}\Delta\mathbf{x} + \mathbf{B_i}\Delta\mathbf{u} \tag{3.72}$$

$$\Delta\mathbf{y} = \mathbf{C_i}\Delta\mathbf{x} \tag{3.73}$$

where:

$$\mathbf{A_i} = \begin{bmatrix} -L_{11}^{-1} r_s & -L_{12}^{-1} r_s & -L_{13}^{-1} r_s \\ -L_{21}^{-1} r_s & -L_{22}^{-1} r_s & -L_{23}^{-1} r_s \\ -L_{31}^{-1} r_s & -L_{32}^{-1} r_s & -L_{33}^{-1} r_s \end{bmatrix}, \quad \mathbf{B_i} = \begin{bmatrix} L_{11}^{-1} \bar{V}_b & L_{12}^{-1} \bar{V}_b & L_{13}^{-1} \bar{V}_b \\ L_{21}^{-1} \bar{V}_b & L_{22}^{-1} \bar{V}_b & L_{23}^{-1} \bar{V}_b \\ L_{31}^{-1} \bar{V}_b & L_{32}^{-1} \bar{V}_b & L_{33}^{-1} \bar{V}_b \end{bmatrix} \tag{3.74}$$

The output matrix is chosen as:

$$\mathbf{C_i} = \begin{bmatrix} 1 & 0 & 0 \\ 0 & 1 & 0 \\ 0 & 0 & 1 \end{bmatrix} \tag{3.75}$$

To eliminate steady-state tracking error and ensure balanced phase currents, the system is augmented with three integral, see Section 2.3.2. The augmented state-space representation is therefore given by

$$\bar{\mathbf{A}}_{inner} = \begin{bmatrix} \mathbf{A}_i & \mathbf{0}_{3\times3} \\ -\mathbf{C}_i & \mathbf{0}_{3\times3} \end{bmatrix}, \quad \bar{\mathbf{B}}_{inner} = \begin{bmatrix} \mathbf{B}_i \\ \mathbf{0}_{3\times3} \end{bmatrix} \tag{3.76}$$

The optimal control input is obtained through an LQR formulation, see Section 3.3.5.1, where the control law minimises the quadratic cost functional:

$$J = \int_0^\infty (x_{aug}^T Q x_{aug} + u^T R u) dt \tag{3.77}$$

The resulting control law is expressed as:

$$\mathbf{u}(t) = \mathbf{K}_p(x_{ref} - x_{measured}) + \mathbf{K}_i \int_0^t (x_{ref} - x_{measured})\, dt + \mathbf{u}_{ff}(t) \tag{3.78}$$

where:

- $\mathbf{K}_p$ denotes the proportional gain matrix obtained from the state-feedback component of the LQR gain matrix;
- $\mathbf{K}_i$ denotes the integral gain matrix associated with the augmented integral states;
- $\mathbf{u}_{ff}(t)$ represents the steady-state feedforward compensation term.

3.3.3.2 Controllability Verification

Following the integral augmentation, tthe controllability of the augmented system is verified to ensure that all states are reachable from the control input. This is assessed with the reachability matrix:

$$\mathbf{W}_{r_i} = \begin{bmatrix} \bar{\mathbf{B}}_{inner} & \bar{\mathbf{A}}_{inner}\bar{\mathbf{B}}_{inner} & \bar{\mathbf{A}}_{inner}^2\bar{\mathbf{B}}_{inner} & \cdots & \bar{\mathbf{A}}_{inner}^6\bar{\mathbf{B}}_{inner} \end{bmatrix} \tag{3.79}$$

Evaluation of the matrix rank using the MATLAB rank() function yields

$$rank(\mathbf{W}_{r_i}) = 6 \tag{3.80}$$

which is equal to the total number of augmented system states. The system is therefore fully controllable, implying that each state variable can be independently influenced through the control input.

3.3.4 Outer-Loop SISO Voltage Control

3.3.4.1 System Formulation, Matrix Decoupling, and Integral Augmentation

The outer control loop regulates the input capacitor voltage $V_{C_{in}}$ by treating the total phase current as the control input. To facilitate the controller synthesis, the voltage dynamics are isolated from the full system representation and expressed in state-space form as:

$$\Delta x = \left[\Delta V_{C_{in}}\right], \qquad \Delta u = \left[\Delta I_{sum}\right]. \tag{3.81}$$

The total phase current is defined as:

$$\Delta I_{sum} = \Delta i_a + \Delta i_b + \Delta i_c \tag{3.82}$$

The corresponding linearised dynamics are expressed as:

$$\Delta \dot{x} = A_v \Delta x + B_v \Delta u \tag{3.83}$$

$$\Delta y = C_v \Delta x \tag{3.84}$$

where:

$$A_v = \left[0\right], \qquad B_v = \left[-\frac{1}{C_{in}}\right] \tag{3.85}$$

The output matrix is chosen as:

$$C_v = \left[1\right] \tag{3.86}$$

To eliminate steady-state voltage tracking error, the system is augmented with a single integral state, see Section 2.3.2. The augmented state-space representation is therefore given by:

$$\bar{\mathbf{A}}_{outer} = \begin{bmatrix} A_v & 0 \\ -C_v & 0 \end{bmatrix}, \quad \bar{\mathbf{B}}_{outer} = \begin{bmatrix} B_v \\ 0 \end{bmatrix} \tag{3.87}$$

The resulting control law is expressed as:

$$I_{sum}(t) = K_p(x_{ref} - x_{measured}) + K_i \int_0^t (x_{ref} - x_{measured}), dt + I_{ff}(t) \tag{3.88}$$

where:

- K_p denotes the proportional gain obtained from the pole placement of the inner-loop LQR controller;
- K_i denotes the integral gain associated with the augmented integral state;
- $I_{ff}(t)$ represents the feedforward compensation term.

3.3.4.2 Controllability Verification

Following the integral augmentation, the controllability of the augmented system is verified to ensure that all states are reachable from the control input. This is assessed with the reachability matrix:

$$\mathbf{W}_{r_v} = \begin{bmatrix} \bar{\mathbf{B}}_{outer} & \bar{\mathbf{A}}_{outer}\bar{\mathbf{B}}_{outer} \end{bmatrix} \tag{3.89}$$

Evaluation of the matrix rank using the MATLAB rank() function yields

$$rank(\mathbf{W}_{r_v}) = 2 \tag{3.90}$$

which is equal to the total number of augmented system states. The system is therefore fully controllable, implying that each state variable can be independently influenced through the control input.

3.3.5 Tuning via LQR and Pole Placement

The Linear Quadratic Regulator (LQR) is used to optimally tune the inner-loop current controller. This tuning approach minimises the controller search space while providing the precise control required for regulating the stator winding currents. LQR is particularly suitable for the coupled (6x6) current MIMO system, as it produces an optimal closed-loop response while also providing information about the resulting pole locations.

The pole locations of the tuned inner current loop are then used as the reference point for designing the slower outer voltage loop. For the outer loop, a pole placement approach is employed. The reason for selecting LQR for the inner current loop and pole placement for the outer voltage loop is that the current loop behaviour must be highly precise, and LQR avoids the need to manually search through a large set of possible pole locations to achieve the desired response.

Since the outer voltage controller is inherently connected to the inner current controller, but operates on a slower timescale, the known closed-loop poles of the current controller can be used to efficiently tune the voltage controller to be approximately ten times slower. The voltage loop reduces to a simpler (2x2) augmented SISO integrator system. Because this outer-loop system is highly predictable, pole placement is preferred over LQR.

3.3.5.1 LQR MIMO Stator Current

Using Bryson's Rule, the weighting matrices are constructed directly from the maximum acceptable state deviations and control effort. Each weight is chosen as the inverse square of its corresponding physical limit. The selected tolerances used for Bryson's Rule are shown in Table 3.4.

Table 3.4: Bryson Rule Tuning Limits

Parameter	Maximum Acceptable Value
Current tracking error ($i_{\text{acceptable}}$)	$(i_{\text{acceptable}})_{\max} = 1$
Integral current error ($\int i_{\text{acceptable}}$)	$(\int i_{\text{acceptable}})_{\max} = 1 \times 10^{-4}$
Duty-cycle variation (ΔD)	$\Delta D_{\max} = 1 \times 10^{-4}$

$$Q_i = \frac{1}{(i_{\text{err,max}})^2} \tag{3.91}$$

$$Q_{\int i} = \frac{1}{((\int i_{\text{err}})_{\max})^2} \tag{3.92}$$

$$R_{\Delta d} = \frac{1}{(\Delta D_{\max})^2} \tag{3.93}$$

$$\mathbf{Q} = \begin{bmatrix} Q_i & 0 & 0 & 0 & 0 & 0 \\ 0 & Q_i & 0 & 0 & 0 & 0 \\ 0 & 0 & Q_i & 0 & 0 & 0 \\ 0 & 0 & 0 & Q_{\int i} & 0 & 0 \\ 0 & 0 & 0 & 0 & Q_{\int i} & 0 \\ 0 & 0 & 0 & 0 & 0 & Q_{\int i} \end{bmatrix} \tag{3.94}$$

$$\mathbf{R} = \begin{bmatrix} R_{\Delta d} & 0 & 0 \\ 0 & R_{\Delta d} & 0 \\ 0 & 0 & R_{\Delta d} \end{bmatrix} \tag{3.95}$$

The optimal state-feedback gain is obtained by solving the continuous-time algebraic Riccati equation:

$$\mathbf{A}^T\mathbf{P} + \mathbf{P}\mathbf{A} - \mathbf{P}\mathbf{B}\mathbf{R}^{-1}\mathbf{B}^T\mathbf{P} + \mathbf{Q} = 0 \tag{3.96}$$

where $\mathbf{P}$ is a positive definite matrix representing the optimal cost-to-go function. The optimal feedback gain matrix is then given by:

$$\mathbf{K}_{LQR} = \mathbf{R}^{-1}\mathbf{B}^T\mathbf{P} \tag{3.97}$$

In practice, this convex optimisation problem is solved numerically using MATLAB via the `lqr` function, which directly returns the optimal feedback gain matrix.

$$\mathbf{K}_{LQR} = \begin{bmatrix} 0.0006 & 0 & -0.0001 & -1.0000 & 0 & 0 \\ 0 & 0.0005 & 0 & 0 & -1.0000 & 0 \\ -0.0001 & 0 & 0.0006 & 0 & 0 & -1.0000 \end{bmatrix} \tag{3.98}$$

The resulting gain matrix ($K_{\text{LQR}} \in \mathbb{R}^{3\times 6}$) contains feedback gains associated with both the current-error states and the integral-error states. The gain matrix is partitioned into proportional and integral components.

The proportional part:

$$\mathbf{K}_{P_{Current}} = 10^{-}3 \begin{bmatrix} 0.5835 & -0.0134 & -0.1368 \\ -0.0134 & 0.4602 & -0.0134 \\ -0.1368 & -0.0134 & 0.5835 \end{bmatrix} \tag{3.99}$$

The integral part:

$$\mathbf{K}_{I_{Current}} = \begin{bmatrix} -1.0 & -0.0 & -0.0 \\ -0.0 & -1.0 & 0.0 \\ 0.0 & -0.0 & -1.0 \end{bmatrix} \tag{3.100}$$

3.3.5.2 Pole Placement SISO Outer Voltage Control

The outer voltage controller is inherently connected to, and dependent upon, the behaviour of the inner current-control loop. Therefore, the poles obtained from the LQR-tuned current controller can be used as a starting point for tuning the outer voltage controller. By leveraging pole-placement techniques, the outer loop can be designed to be approximately one order of magnitude slower than the inner loop, ensuring adequate time-scale separation and preventing undesirable interaction between the two control loops.
After obtaining the $(3 \times 6\ )$ LQR gain matrix, the closed-loop inner current-control system is constructed as:

$$\mathbf{A}_{\text{cl,inner}} = \mathbf{A}_i - \mathbf{B}_i \mathbf{K}_{\text{LQR}} \tag{3.101}$$

The closed-loop eigenvalues are then computed using MATLAB's `eig` function:

$$\boldsymbol{\lambda}_{\text{inner}} = 10^3 \begin{bmatrix} -1.3934 + 1.3668i \\ -1.3934 - 1.3668i \\ -2.3709 + 2.2462i \\ -2.3709 - 2.2462i \\ -2.1551 + 2.0602i \\ -2.1551 - 2.0602i \end{bmatrix} \tag{3.102}$$

For the purpose of tuning the outer voltage controller, the dominant poles associated with the proportional and integral actions are identified as:

$$\boldsymbol{\lambda}_{\text{P}} = 10^3 \begin{bmatrix} -1.3934 + 1.3668i \\ -1.3934 - 1.3668i \\ -2.3709 + 2.2462i \end{bmatrix} \tag{3.103}$$

$$\boldsymbol{\lambda}_{\text{I}} = 10^3 \begin{bmatrix} -2.3709 - 2.2462i \\ -2.1551 + 2.0602i \\ -2.1551 - 2.0602i \end{bmatrix} \tag{3.104}$$

These eigenvalues define the pole locations of the inner current-control loop. The poles closest to the imaginary axis represent the slowest system dynamics and are therefore used as the reference point for the outer voltage-loop design. By selecting the outer-loop poles to be significantly slower than the inner-loop poles, the current

controller can be assumed to have reached steady state before the voltage controller responds, thereby maintaining proper loop decoupling.
The reference pole locations used as the starting point for the voltage-controller tuning process are summarised in Table 3.5.

Table 3.5: Reference pole locations used for voltage-controller pole-placement tuning

Voltage Controller Tuning	**Reference Pole Location From LQR**
Proportional Part (P)	$P_O = (-1.3934)10^3$
Integral Part (I)	$I_O = (-2.1551)10^3$

3.3.6 Feedforward Design

The Jacobian linearisation relies on localised small-signal approximations, a linear controller can struggle or saturate during massive transient shocks, such as a severe drop in station current or station voltage. To mitigate this limitation, a large-signal model-based feedforward term is calculated based on the ideal boost converter equilibrium. We can use the fundamental boost relationship in Equation 3.105 to derive the duty cycle feedforward shown in Equation 3.106:

$$V_{out} = \frac{1}{1-D} V_{in} \tag{3.105}$$

$$D_{ff} = 1 - \frac{V_{C_{in}}}{V_{battery}} \tag{3.106}$$

Similarly, the current feedforward is obtained by taking the direct station current measurement and feeding that information forward to the controller, as shown in Equation 3.107:

$$I_{ff} = I_{station} \tag{3.107}$$

This term handles the coarse, large-signal voltage lift required across the booster, leaving the feedback state-space controllers to manage only small-signal dynamic corrections and localised disturbances.

3.4 Verification Framework

3.4.1 Open-Loop Oscillation Frequency

The interaction between the charging station cable impedance, the stator winding network, and the input smoothing capacitor (C_{in}) forms an underdamped RLC resonant circuit. The characteristic natural frequency of this network, including the rotor-angle-dependent inductance, is bounded by:

$$f(\theta_e) = \frac{1}{2\pi} \sqrt{-\frac{1}{C_{\text{in}} D(\theta_e)} - \frac{r_s^2}{\left(2D(\theta_e)\right)^2}} \tag{3.108}$$

where

$$D(\theta_e) = L_\delta \Big[\cos(2p\theta_e) + \cos\left(\frac{2\pi}{3} - 2p\theta_e\right) + \cos\left(\frac{2\pi}{3} + 2p\theta_e\right) \Big] - L_{\text{ls}} \tag{3.109}$$

When an open-loop step change in duty cycle is applied, this underdamped system gives rise to pronounced oscillations in both the phase currents and the input voltage. To assess the accuracy of the open-loop state-space model against the independent circuit simulations, the transient peak-to-peak response is evaluated. This allows verification that the dominant oscillation frequencies observed in simulation are consistent with those predicted by the analytical expression for $f(\theta_e)$.

3.4.2 Open Loop plant model verification

To validate the state-space model developed in this work, a three-step verification and validation framework is employed. First, the correctness of the linearisation is assessed by comparing the linear state-space representation with the nonlinear plant model, expressed in transfer function form. This provides an initial verification that the linear model accurately represents the underlying nonlinear system dynamics.

Secondly, the state-space model is validated against and further compared with an independent circuit-level simulation, see Figure 3.3. Across all three representations, consistent system responses are expected for variations in duty-cycle input and across different operating points. This open-loop validation is performed using a duty-cycle perturbation sweep and sequential sweep across operating points, see Figure 4.1.

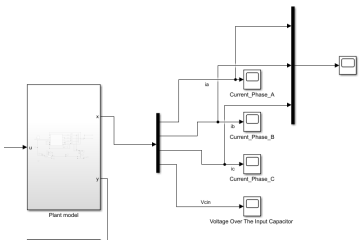

(a) Nonlinear state-space plant

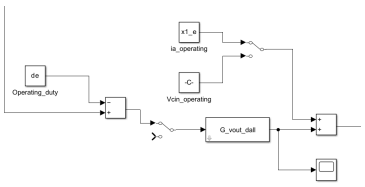

(b) Linearised plant (transfer function model)

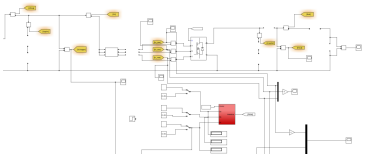

(c) Independent circuit model

Figure 3.3: Open-loop validation comparing (a) nonlinear state-space plant, (b) linearised transfer function model, and (c) independent circuit simulation.

3.4.3 Closed Loop State Space Controller verification

The second stage of validation focuses on discretisation effects and controller implementation. In this stage, the performance of the controller is compared between the continuous-time averaged state-space model and a naturally discretised model that emulates digital implementation behaviour (the independent circuit simulation), see Figure 3.4. The expected outcome is that both representations exhibit equivalent closed-loop performance, confirming that the controller is robust across different modelling environments. Furthermore, this validates that the sampling rate is sufficiently high such that discretisation does not introduce any significant shift in the system poles.

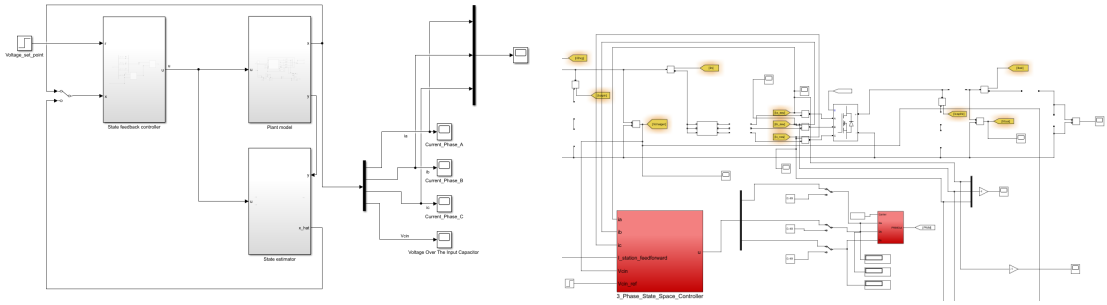

(a) Averaged state-space model with controller

(b) Circuit model with identical controller implementation

Figure 3.4: Closed-loop comparison between the developed state-space model and an independent circuit simulation

3.4.4 Control Robustness

The controller is designed around a suitable operating point using the basic boost converter equation. In addition, the controller is designed to account for the worst-case rotor angle, corresponding to the condition where the inductance is at its lowest value. The controller performance is then evaluated by analysing the system both with and without feedforward terms. Several worst-case scenarios are considered, including the largest expected variation in battery voltage during charging and the maximum power variation, which corresponds to the highest current change demanded from the station, see Table 3.6. Finally, the robustness of the controller is assessed under voltage disturbances by increasing the reference voltage from 400 V to 500 V, thereby evaluating its ability to handle sudden changes in the supply voltage.

Table 3.6: Controller robustness, worst-case validation scenarios

Case	**Values**
Worst-Case Rotor Angle	30 deg
Feedforward Evaluation	$I_{ff} = 0$ & $D_{ff} = 0$
Battery Voltage Variation	$\Delta 5V$
Power Demand Variation	$\Delta 10A$
Voltage Disturbance Test	$\Delta 100V$

4

Results

4.1 Open-Loop Plant Model

A two-step open-loop verification procedure is carried out to validate the proposed plant model. First, the transfer function obtained from the linearised state-space model is compared against the nonlinear mathematical plant model. Second, the same transfer function is validated against an independent circuit-level simulation model. This approach ensures the validity of the plant model and confirms that no mathematical errors were introduced during the linearisation process. The verified model is then used as the basis for controller design.

4.1.1 RLC Resonant Dynamics

The open-loop responses from both the circuit model and the average state-space model exhibits damped oscillations. This behaviour is inherently due to the RLC nature of the circuit, where the duty cycle pulses trigger the system's natural resonant response. By analysing the peak-to-peak intervals of these oscillations, a clear correlation to the natural resonance frequency of the RLC circuit is established. This relationship is verified by the calculated theoretical frequency and the observed peak-to-peak frequency being congruent. The mathematical formulation for this resonance frequency, as a function of the electrical angle θ_e, is defined in equation 3.108.

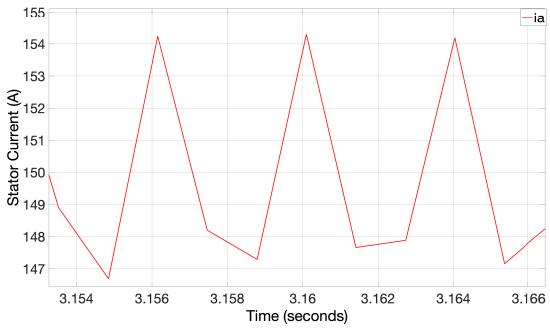

(a) System Oscillation

▼ Peaks

	Value	Time (seconds)
☑	1.543e+02	3.160
☑	1.542e+02	3.156
☑	1.542e+02	3.164

(b) Peak Finder Data

Figure 4.1: The Oscillation Frequency Corresponds to the Natural LC Resonance Frequency of the System.

4.1.2 Plant Model Validation

The nonlinear DC-DC booster exhibits weak affine nonlinearity during the charging interval because the rotor position remains approximately constant. Although the rotor angle may assume an arbitrary initial value before charging begins, its variation during charging is negligible. The affine system is subsequently linearised around the nominal operating point.
The open-loop validation therefore, serves both as a validation of the mathematical model and as an assessment of the validity range of the linear approximation. To evaluate this range, the duty cycle is swept from values significantly above the nominal operating point of $D = 0.5$ downwards over a duration of 1.5 s. The results show that the linearised model deviates from the nonlinear model for large duty-cycle variations, particularly for unrealistic duty change such as $\Delta D = 0.1$. However, as the operating point approaches the linearisation point, the agreement between the models improves significantly, confirming the validity of the linear approximation for practical operating conditions. The table shows our two distinct duty sweeps. We can also see in Figure 4.2 that the change in duty does not give identical current reaction in our symmetrical stator. This is due to the eddy current effect at our operating frequency and subsequently rotor angle dependent induction.
Figures B.3–4.1 compare the nonlinear state-space model and the linearised transfer-function model. The responses demonstrate strong agreement in both the capacitor voltage and stator current dynamics near the nominal operating region.

Table 4.1: Applied duty-cycle sweep sequences used for state space model validation

Sweep Type	**Duty-Cycle Sequence**
Sequential sweep	$D = 0.1 \rightarrow 0.9,\ \Delta D = 0.1,\ 0.9 \rightarrow 0.1$
Perturbation sweep	$D = 0.5 \pm \Delta D,\ \Delta D = [0.1,\ 0.05,\ 0.025,\ 0.01]$

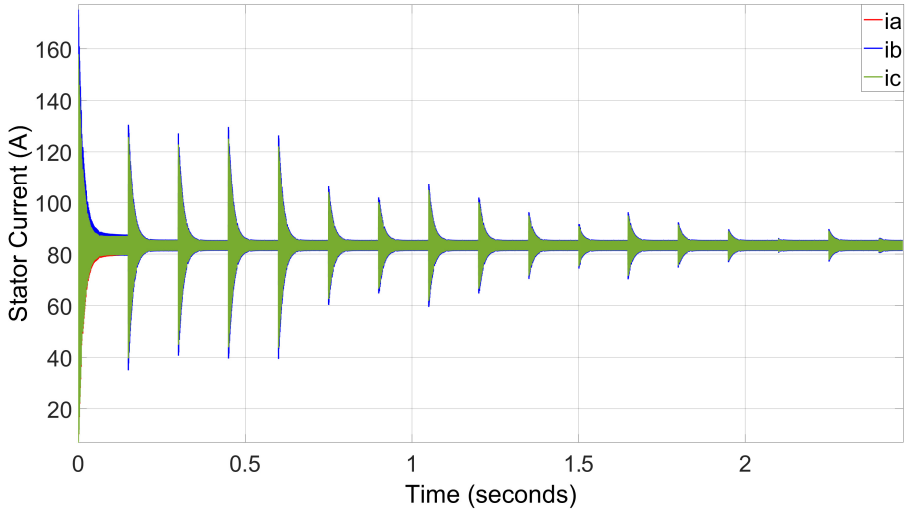

Figure 4.2: Open-loop response of stator currents during duty cycle sweep.

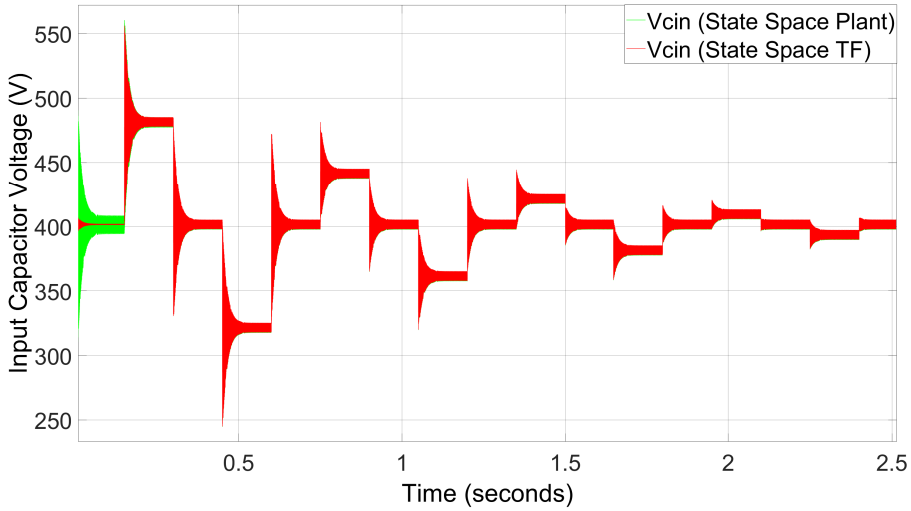

Figure 4.3: Open-loop verification comparing the linearised transfer function and nonlinear state-space plant for input capacitor voltage dynamics.

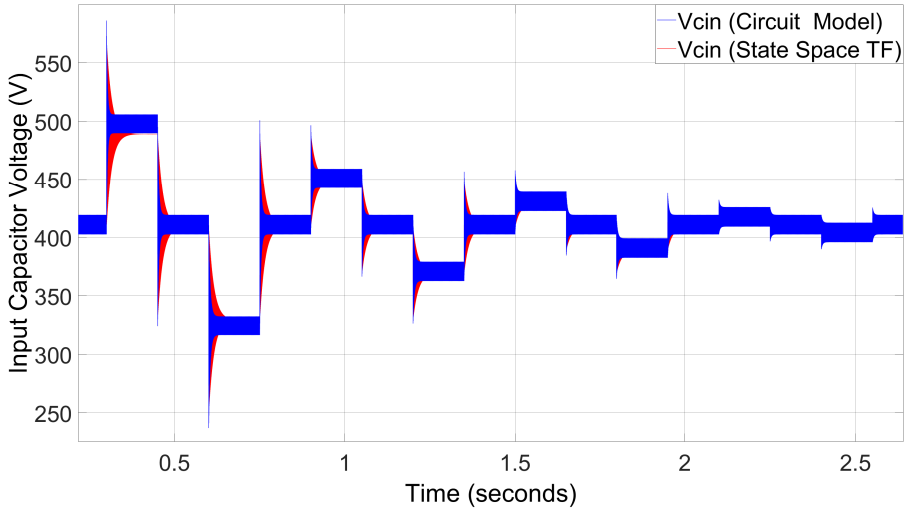

Figure 4.4: Open-loop validation comparing the state-space and circuit models for input capacitor voltage dynamics.

A similar verification of our two-phase and single-phase state-space model phase shedding method is carried out using an independent circuit model, and the results are presented in Appendix C.

4.1.3 Bode

Figure 4.5 shows that the phase lag is limited to $-90°$, which is well away from the critical $-180°$ condition required for oscillatory instability. The system also exhibits a high DC gain of approximately 95 dB, indicating strong sensitivity of the current response to duty cycle variations at low frequencies, which is beneficial for current regulation.

From a control design perspective, this provides a comfortable phase margin, allowing the use of a PI current controller without risking instability, provided that the crossover frequency is chosen sufficiently below the switching frequency.

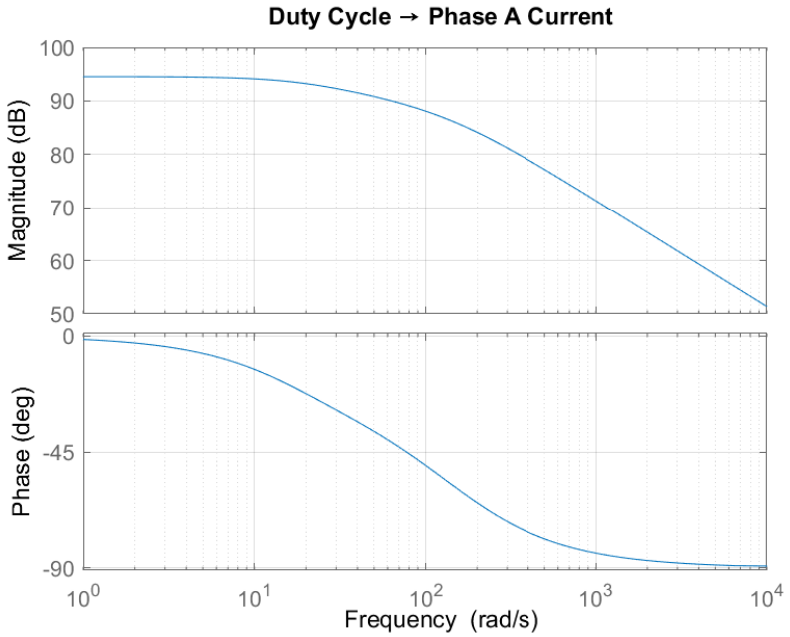

Figure 4.5: Bode plot showing the system stability margin.

4.2 Cascade Control Architecture

4.2.1 Inner-Loop MIMO Current Control Performance

The inner current control loop is designed and tuned using an LQR-based state-feedback approach. The resulting controller rapidly eliminates steady-state error and achieves a stator current settling time of approximately 5 ms. This response is intentionally selected to remain slower than the MOSFET switching dynamics while still being sufficiently fast to react to voltage controller demands, thereby preventing voltage overshoot and minimising transient voltage spikes.

The tuned controller is subsequently implemented in a detailed circuit-level simulation, which inherently exhibits discrete switching behaviour due to the on/off operation of the power semiconductors. The results demonstrate an excellent agreement between the averaged state-space model and the switching circuit model, confirming the validity of the control design and its dynamic performance, see Figure 4.6.

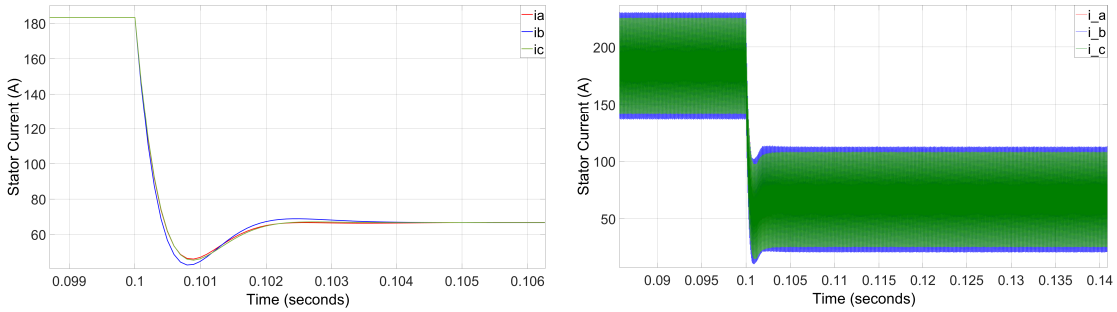

(a) Averaged state-space mode **(b)** Detailed switching circuit model

Figure 4.6: Comparison of stator current response under current control for the averaged state-space and detailed switching circuit models.

4.2.2 Outer-Loop SISO Voltage Control Performance

Following the LQR and pole-placement-based tuning of the cascade control structure, the voltage loop response is evaluated under step changes in the reference setpoint. The voltage control loop exhibits a response time of approximately 50 ms, making it roughly an order of magnitude slower than the inner current control loop. This separation of time scales ensures proper cascade operation and enhances system stability by allowing the inner loop to settle significantly faster than the outer loop dynamics.

The tuned controller is implemented in a circuit-level simulation that includes switching effects, resulting in a naturally discrete-time behaviour. The simulation results show close agreement between the averaged model and the switching circuit model, further validating the accuracy of the Modelling approach and controller design.

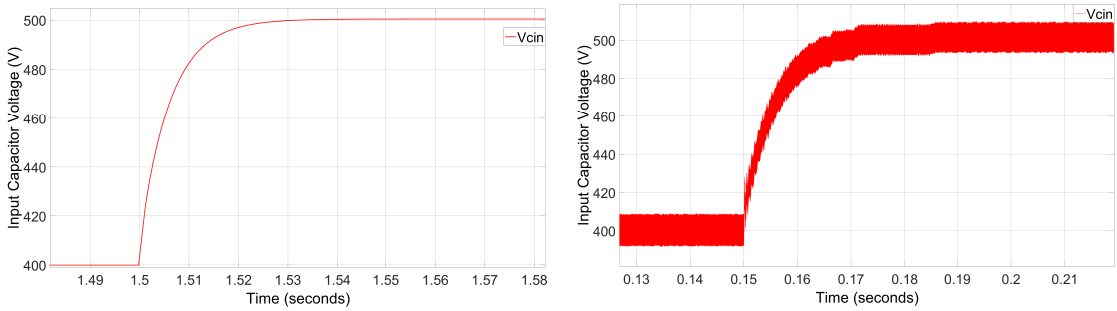

(a) Averaged state-space mode **(b)** Detailed switching circuit model

Figure 4.7: Comparison of input capacitor voltage response under voltage control using the averaged state-space model and the detailed switching circuit model.

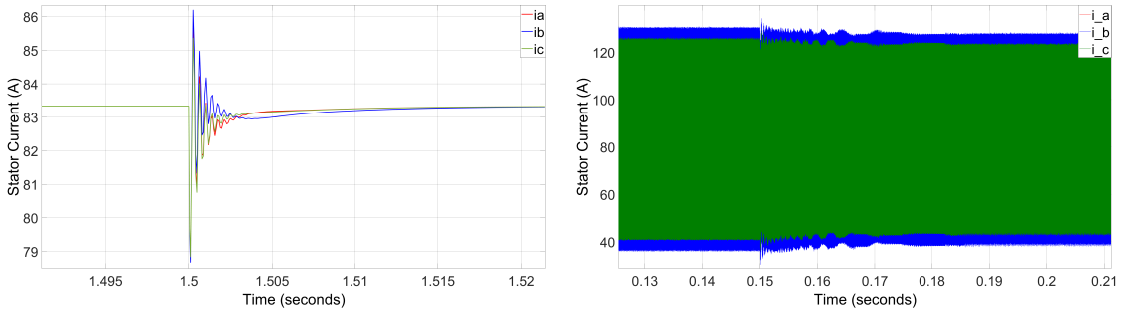

(a) Averaged state-space mode **(b)** Detailed switching circuit model

Figure 4.8: Comparison of stator current response under voltage control using the averaged state-space model and the detailed switching circuit model.

4.2.3 Feedforward Design

The feedforward design plays a key role in the overall control response, as it accounts for the majority of the control effort, see Figure 4.9. When accurate feedforward values are used, the feedback controller is only required to correct small deviations, thereby reducing the observed error. By incorporating known system information, such as the station current level and an approximate duty cycle ratio, the controller can operate less aggressively while achieving improved overall performance.

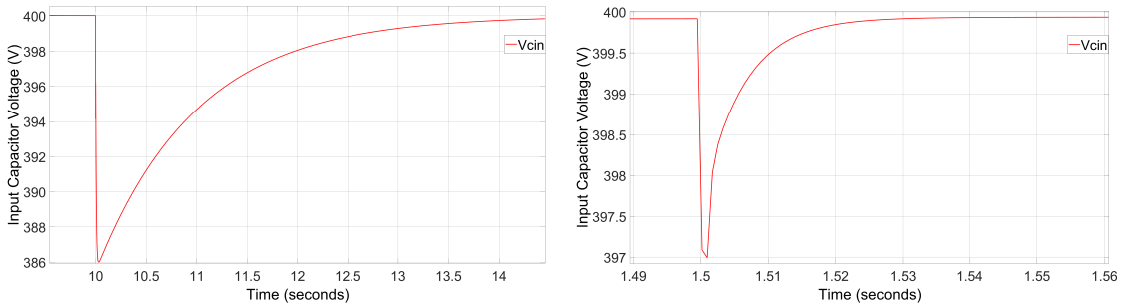

(a) Without feedforward **(b)** With feedforward

Figure 4.9: Effect of feedforward compensation on voltage recovery performance.

4.3 Control Robustness

4.3.1 Station Power Reduction

As the battery transitions from a low state of charge to full charge, the required power from the station gradually decreases. Consequently, the requested current is reduced progressively. Although this variation is gradual in practice, a worst-case scenario can be tested by applying a step decrease in station current to verify controller performance, see Figure 4.10. The results confirm that the controller remains stable and performs as intended.

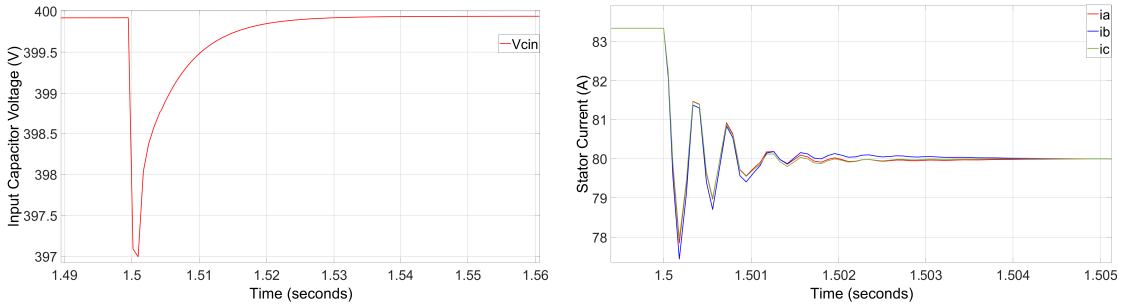

(a) Response of the voltage controller **(b)** Response of the current controller

Figure 4.10: Voltage and current controller responses following a step reduction in station power demand.

4.3.2 Battery Voltage Variation

As the battery charges and the state of charge increases, the battery voltage also rises. However, these dynamics are very slow, with the largest observed step change being less than 2 V. This variation has no significant impact on controller performance, and the system remains stable throughout the charging process, see Figure 4.11.

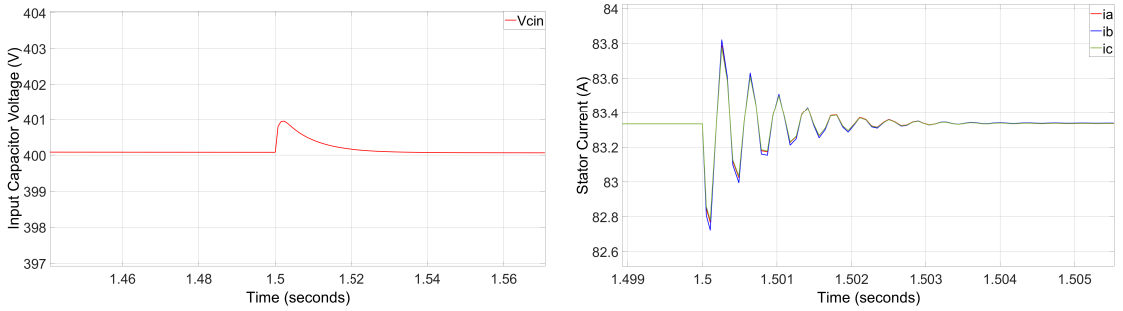

(a) Response of the voltage controller **(b)** Response of the current controller

Figure 4.11: Voltage and current controller responses following a step increase in battery voltage.

4.3.3 Rotor Position Sensitivity

The controller is designed for the worst-case operating condition, corresponding to a rotor angle of (30°), which results in the lowest inductance in the three-phase stator windings. By designing for this minimum-inductance case, robust operation is ensured across the full (360°) range of possible rotor positions. Figures 4.12–4.14 demonstrate that the controller performs as intended for different rotor angles. Despite the variation in machine inductance caused by changes in rotor position, the controller remains stable and maintains satisfactory dynamic performance.

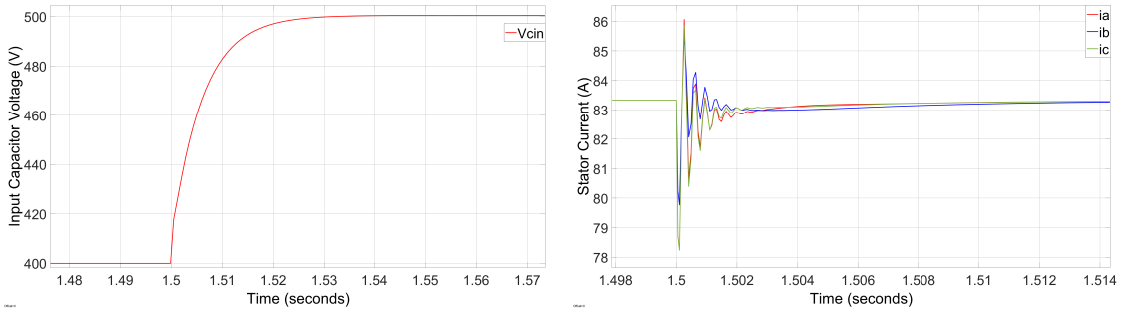

(a) Response of the voltage controller **(b)** Response of the current controller

Figure 4.12: Voltage and current controller responses at a rotor angle of 0° following a step increase in the voltage reference.

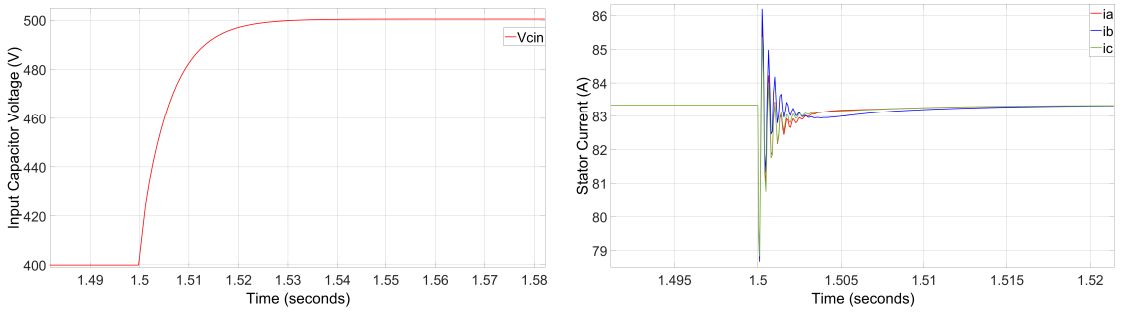

(a) Response of the voltage controller **(b)** Response of the current controller

Figure 4.13: Voltage and current controller responses at a rotor angle of 30° following a step increase in the voltage reference.

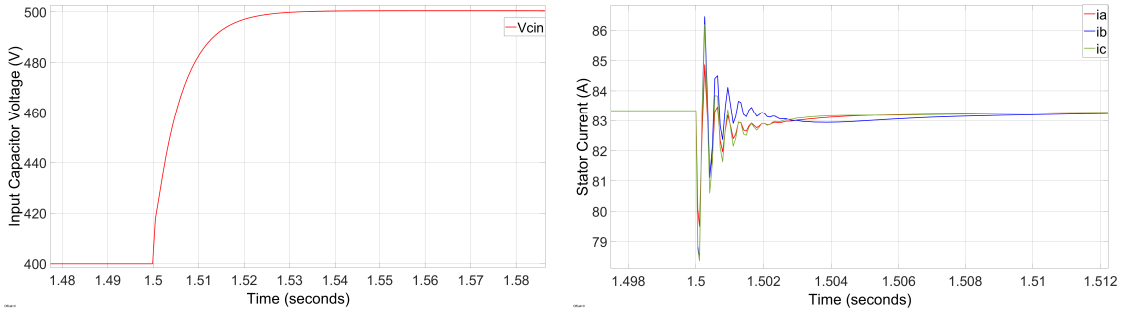

(a) Response of the voltage controller **(b)** Response of the current controller

Figure 4.14: Voltage and current controller responses at a rotor angle of 60° following a step increase in the voltage reference.

4.3.4 Discontinuous Conduction Mode (DCM)

The majority of the charging duration operates in continuous conduction mode; therefore, the state-space model is designed for this operating condition. However,

towards the end of charging, when less power is required from the station, the system may enter discontinuous conduction mode, during which the current in the stator windings falls to zero during the boost interval.
The controller response under this operating condition can then be observed in Figure 4.15.

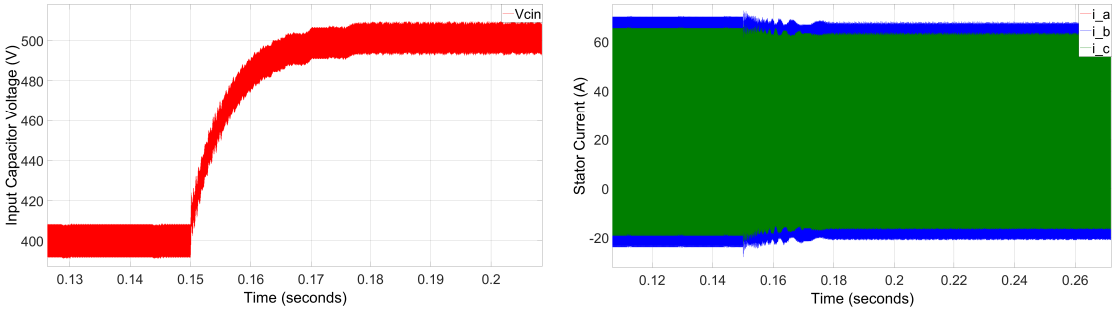

(a) Response of the voltage controller **(b)** Response of the voltage controller

Figure 4.15: The cascaded voltage and current controllers in the circuit simulation under discontinuous conduction mode (DCM) following a step change in the voltage reference.

5

Conclusion

5.1 Discussion of Methodology

The booster is a nonlinear system, and the degree of nonlinearity increases if the rotor position is allowed to vary during charging. By effectively keeping the rotor angle fixed during operation, the system complexity is reduced and the model becomes affine with weak input nonlinearity.

Using the inverse Clarke–Park transformation, it can be shown that maintaining equal phase currents should prevent the generation of steady-state torque. However, no direct torque measurements were taken, and no torque simulations were performed. Although existing literature and the Clarke–Park transformation suggest that the controller should eliminate steady-state error in the stator windings, this cannot be stated as a definitive guarantee in the present work.

Cascade control provides an effective means of decoupling a system that cannot be fully controlled using a single state-space controller. The controllability analysis of the full 8×8 system matrix indicates limitations in direct single-loop control. By introducing a cascade structure with time-scale separation, the system is decomposed into a 6×6 and a 2×2 subsystem. This approach improves controllability and enables the system to achieve the desired control objectives.

5.2 Discussion of Results

We observe that the controller performance is essentially identical in both the continuous-time state-space model and the discretised switching (on/off) circuit implementation. This is mainly due to the high switching frequency, where a smaller sampling interval leads to reduced deviation from the continuous-time (analogue) behaviour. In this case, the fast switching is beneficial, as the sampling time is sufficiently small that it does not significantly affect the system dynamics or shift the system poles in any meaningful way.

During discontinuous conduction mode (DCM) the circuit model shows it that the current drops to zero and even becomes negative. This indicates that power is temporarily flowing from the battery back to the station during the charging process, despite the presence of a MOSFET body diode. A controller designed for continuous conduction mode (CCM) is not recommended for operation in DCM. In general, it is preferable to avoid entering DCM during charging whenever possible.

5.3 Concluding Remarks

The state-space model is a valuable tool in the development process. If parameters such as capacitor value, battery voltage, or the electrical machine air-gap change, the same control structure can be adapted with minimal effort from the research and development team. This supports the OEM development cycle by reducing the need for repeated iterative tuning and redesign whenever changes to the system are introduced.
We have achieved a well-tuned, physics-aware controller that can boost the voltage, avoid voltage spikes in the capacitors, and regulate the desired current in the stator windings. This allows the system to maintain the required voltage without inducing steady-state torque in the electrical machine (IPMSM).

6
Future Work

At the end of the charging process, when the required power from the charging station decreases, the system may enter Discontinuous Conduction Mode (DCM). This behaviour should either be avoided or explicitly accounted for through an extension of the present model.
The introduction of three-phase interleaved PWM improves output current quality and reduces stress on the output capacitor and battery by lowering current ripple. However, under interleaved operation, the conventional method of estimating average current using ripple peak and valley measurements is no longer valid. This is due to the 120° phase-shifted current components, which distort the apparent ripple profile.
To address this limitation, a corrected current estimation method is required. The measured phase currents must be compensated using machine parameters such as mutual inductance, leakage inductance, and the saliency constant, as these directly influence phase coupling and ripple behaviour under high-frequency switching.
The proposed correction is based on phase-dependent compensation terms derived from machine parameters and operating conditions. The full current correction function is provided in Appendix D.3.
This approach provides a basis for improved current reconstruction under interleaved operation and should be further validated experimentally, alongside system-level parameter identification. It is also of interest to investigate the trade-off associated with allowing DCM operation during the final charging stage, particularly in terms of efficiency, control complexity, and potential impact on vehicle range.
Future work should focus on:

- Development of a DCM state-space model and its integration via gain scheduling with the CCM model, or alternatively enforcing CCM operation during the final charging stage.
- Experimental identification of mutual inductance, leakage inductance, and saliency constants at the actual switching frequency.
- Implementation and validation of a corrected current sampling strategy for three-phase interleaved PWM systems.

Bibliography

[1] Y. Hwang, J. Kim, M. Lee, J. Choi, and K. Nam, "Phase current equalization method of ipmsm-based on-board boost converter for electric vehicles," *IEEE Access*, vol. 13, pp. 121 533–121 543, 2025.

[2] S.-K. Sul, *Control of Electric Machine Drive Systems*. IEEE Press, 2010, published via IEEE Xplore Digital Library.

[3] F. D. B. Albuquerque, M. A. Maraqa, R. Chowdhury, T. Mauga, and M. Alzard, "Greenhouse gas emissions associated with road transport projects: Current status, benchmarking, and assessment tools," *Transportation Research Procedia*, vol. 48, pp. 2018–2030, 2020. [Online]. Available: https://www.sciencedirect.com/science/article/pii/S2352146520306803

[4] S. Jaman, S. Chakraborty, M. E. Baghdadi, T. Geury, and O. Hegazy, "Small-signal average switch modeling and dual-loop control of bidirectional integrated converter for g2v and v2g applications in battery evs," in *2021 23rd European Conference on Power Electronics and Applications (EPE'21 ECCE Europe)*, 2021, pp. 1–12.

[5] Y. Xiao, C. Liu, and F. Yu, "An effective charging-torque elimination method for six-phase integrated on-board ev chargers," *IEEE Transactions on Power Electronics*, vol. 35, no. 3, pp. 2776–2786, 2020.

[6] R. W. Erickson and D. Maksimović, *Fundamentals of Power Electronics*, 3rd ed. Kluwer Academic Publishers, 2001.

[7] N. Ida, *Engineering Electromagnetics*, fourth edition ed. Springer, 2015.

[8] R. Middlebrook, "Small-signal modeling of pulse-width modulated switched-mode power converters," *Proceedings of the IEEE*, vol. 76, no. 4, pp. 343–354, 1988.

[9] M. K. Kazimierczuk, *Pulse-Width Modulated DC-DC Power Converters*, 2nd ed. Chichester, UK: John Wiley & Sons, 2015.

[10] K. J. Åström and R. M. Murray, *Feedback Systems: An Introduction for Scientists and Engineers*. Princeton University Press, 2008.

[11] W. J. Rugh, *Linear System Theory*, 2nd ed. Harlow, UK: Pearson, 2024.

[12] H. K. Khalil, *Nonlinear Systems*, 3rd ed. Upper Saddle River, NJ: Prentice Hall, 2002.

[13] C.-T. Chen, *Linear System Theory and Design*, 3rd ed. New York: Oxford University Press, 1999.

[14] G. F. Franklin, J. D. Powell, and A. Emami-Naeini, *Feedback Control of Dynamic Systems*. Pearson Education, 2019, eighth Edition.

[15] C. C. Paige, "Properties of numerical algorithms related to computing controllability," *IEEE Transactions on Automatic Control*, vol. 26, no. 1, pp. 130–138, 1981.

[16] S. Skogestad and I. Postlethwaite, *Multivariable Feedback Control: Analysis and Design*, 2nd ed. Chichester, UK: John Wiley & Sons, 2005.

[17] M. Ruth, K. Lebsock, and N. Dennehy, "What's new is what's old: Use of bode's integral theorem (circa 1945) to provide insight for 21st century spacecraft attitude control system design tuning," *American Institute of Aeronautics and Astronautics (AIAA) Technical Paper*, 2008, orbital Sciences Corporation / NASA Goddard Space Flight Center.

[18] J. Bryson, Arthur E. and Y.-C. Ho, *Applied Optimal Control: Optimization, Estimation, and Control*. Washington, D.C.: Hemisphere Publishing Corporation, 1975.

[19] A. J. Laub and M. Wette, "Algorithms and software for pole assignment and observers," EE Department, University of California, Santa Barbara, CA, Tech. Rep. UCRL-15646 Rev. 1, Sep. 1984.

[20] J. Kautsky, N. K. Nichols, and P. Van Dooren, "Robust pole assignment in linear state feedback," *International Journal of Control*, vol. 41, pp. 1129–1155, 1985.

[21] J. L. Guzmán and T. Hägglund, *Feedforward Control*. Springer, 2024.

A

Analytical Derivations of System Matrices

This appendix presents the comprehensive symbolic derivations for the various system configuration models developed in this study. The elements L_{ij}^{-1} represent the position-dependent components of the inverted stator inductance matrix, defined directly by:

$$\begin{bmatrix} L_{11}^{-1} & L_{12}^{-1} & L_{13}^{-1} \\ L_{21}^{-1} & L_{22}^{-1} & L_{23}^{-1} \\ L_{31}^{-1} & L_{32}^{-1} & L_{33}^{-1} \end{bmatrix} = \mathbf{L}_{abc}^{-1}(\theta) \tag{A.1}$$

where θ denotes the electrical rotor position. To simplify the row-sum components within the state-space matrices, the following lumped parameters are defined:

$$L_a^{-1} = L_{11}^{-1} + L_{12}^{-1} + L_{13}^{-1}, \quad L_b^{-1} = L_{21}^{-1} + L_{22}^{-1} + L_{23}^{-1}, \quad L_c^{-1} = L_{31}^{-1} + L_{32}^{-1} + L_{33}^{-1} \tag{A.2}$$

A.1 Five-State Non-Linear Plant Model

The most complete physical representation of the IPMSM-based booster includes the full dynamics of both the input and output capacitors. The state vector is defined as $\mathbf{x} = [i_a, i_b, i_c, V_{C_{in}}, V_{C_{out}}]^T$, where i_a, i_b, i_c are the machine phase currents, $V_{C_{in}}$ is the input capacitor voltage, and $V_{C_{out}}$ is the output capacitor voltage.
The non-linear averaged dynamics are governed by the following differential equations:

$$\frac{d\mathbf{i}_{abc}}{dt} = \mathbf{L}_{abc}^{-1}(\theta)\left[\mathbf{v}_{abc} - r_s\mathbf{i}_{abc}\right] \tag{A.3}$$

$$\dot{V}_{C_{in}} = \frac{1}{C_{in}}\left(I_{station} - \sum \mathbf{i}_{abc}\right) \tag{A.4}$$

$$\dot{V}_{C_{out}} = \frac{1}{C_{out}}\left(\sum(1 - \mathbf{D}_{abc})\mathbf{i}_{abc} - \frac{V_{C_{out}} - V_{battery}}{R_{out}}\right) \tag{A.5}$$

where $\mathbf{i}_{abc} = [i_a, i_b, i_c]^T$ is the phase current vector, r_s is the stator winding resistance, C_{in} and C_{out} represent the input and output filter capacitances, $I_{station}$ is the charging station supply current, $V_{battery}$ is the internal nominal battery voltage, R_{out} is the battery-side internal resistance, and $\mathbf{D}_{abc} = [D_a, D_b, D_c]^T$ represents the average phase duty cycle vector. The average phase voltage vector $\mathbf{v}_{abc} = [v_a, v_b, v_c]^T$ is dictated by the switching states and maps to:

$$\mathbf{v}_{abc} = \mathbf{D}_{abc}V_{C_{in}} + (1 - \mathbf{D}_{abc})V_{C_{out}} \tag{A.6}$$

A.2 Linearised 4-State Model (Constant-Current Station)

For control system design, the plant model is reduced to four states by assuming a stiff battery interface ($V_{C_{out}} \approx V_{battery}$). The small-signal state vector $\Delta\mathbf{x}$, control input vector $\Delta\mathbf{u}$, and external disturbance vector $\Delta\mathbf{w}$ are given by:

$$\Delta\mathbf{x} = \begin{bmatrix}\Delta i_a & \Delta i_b & \Delta i_c & \Delta V_{C_{in}}\end{bmatrix}^T, \quad \Delta\mathbf{u} = \begin{bmatrix}\Delta D_a & \Delta D_b & \Delta D_c\end{bmatrix}^T \tag{A.7}$$

$$\Delta\mathbf{w} = \begin{bmatrix}\Delta I_{station} & \Delta V_{battery}\end{bmatrix}^T \tag{A.8}$$

Linearising the system around a steady-state operational equilibrium point $[\bar{\mathbf{x}}, \bar{\mathbf{u}}]$ yields the small-signal system framework:

$$\Delta\dot{\mathbf{x}} = \mathbf{A}_{cc}\Delta\mathbf{x} + \mathbf{B}_{\mathbf{u}}\Delta\mathbf{u} + \mathbf{B}_{w,cc}\Delta\mathbf{w} \tag{A.9}$$

A.2.1 State Matrix $\mathbf{A}_{cc}$

The linearised system state matrix for the constant-current charging configuration is structured as:

$$\mathbf{A}_{cc} = \begin{bmatrix} -L_{11}^{-1}r_s & -L_{12}^{-1}r_s & -L_{13}^{-1}r_s & L_a^{-1} \\ -L_{21}^{-1}r_s & -L_{22}^{-1}r_s & -L_{23}^{-1}r_s & L_b^{-1} \\ -L_{31}^{-1}r_s & -L_{32}^{-1}r_s & -L_{33}^{-1}r_s & L_c^{-1} \\ -\frac{1}{C_{in}} & -\frac{1}{C_{in}} & -\frac{1}{C_{in}} & 0 \end{bmatrix} \tag{A.10}$$

A.2.2 Input and Disturbance Matrices

The control input matrix $\mathbf{B}_{\mathbf{u}}$ and constant-current disturbance matrix $\mathbf{B}_{w,cc}$ are derived as:

$$\mathbf{B}_{\mathbf{u}} = \begin{bmatrix} L_{11}^{-1}\bar{V}_{battery} & L_{12}^{-1}\bar{V}_{battery} & L_{13}^{-1}\bar{V}_{battery} \\ L_{21}^{-1}\bar{V}_{battery} & L_{22}^{-1}\bar{V}_{battery} & L_{23}^{-1}\bar{V}_{battery} \\ L_{31}^{-1}\bar{V}_{battery} & L_{32}^{-1}\bar{V}_{battery} & L_{33}^{-1}\bar{V}_{battery} \\ 0 & 0 & 0 \end{bmatrix}, \quad \mathbf{B}_{w,cc} = \begin{bmatrix} 0 & L_a^{-1}(\bar{D}-1) \\ 0 & L_b^{-1}(\bar{D}-1) \\ 0 & L_c^{-1}(\bar{D}-1) \\ \frac{1}{C_{in}} & 0 \end{bmatrix} \tag{A.11}$$

where $\bar{V}_{battery}$ represents the steady-state operating battery voltage and $\bar{D}$ is the nominal quiescent operating duty ratio.

A.3 Linearised 4-State Model (Constant-Voltage Station)

In the constant-voltage charging mode, the station is modeled as an ideal voltage source $V_{station}$ connected in series with an internal cable resistance R_{in}. Under this configuration, the small-signal disturbance vector transitions to:

$$\Delta\mathbf{w} = \begin{bmatrix}\Delta V_{station} & \Delta V_{battery}\end{bmatrix}^T \tag{A.12}$$

This circuit layout introduces a small-signal damping term a_{44} into the input capacitor voltage dynamics:

$$a_{44} = -\frac{1}{C_{in}R_{in}} \tag{A.13}$$

The resulting system state matrix $\mathbf{A}_{cv}$ remains identical to $\mathbf{A}_{cc}$ except for this modified diagonal element. The updated small-signal disturbance matrix $\mathbf{B}_{w,cv}$ is structured as:

$$\mathbf{B}_{w,cv} = \begin{bmatrix} 0 & L_a^{-1}(\bar{D}-1) \\ 0 & L_b^{-1}(\bar{D}-1) \\ 0 & L_c^{-1}(\bar{D}-1) \\ \frac{1}{C_{in}R_{in}} & 0 \end{bmatrix} \tag{A.14}$$

A.4 Decoupled Augmented Matrices for Control

Because the unified 8x8 small-signal model containing the four physical plant states and four tracking error integral states is rank-deficient, the architecture is separated into an inner-loop and outer-loop cascaded system. This guarantees full rank and controllability for both controller stages.

A.4.1 Inner-Loop: MIMO Phase Current Control (6x6)

The fast inner loop controls the phase currents via an isolated Multiple-Input Multiple-Output (MIMO) system vector $\mathbf{x}_{curr} = [i_a, i_b, i_c]^T$ augmented with three current tracking error integral states to eliminate steady-state offset:

$$\bar{\mathbf{A}}_{curr} = \left[\begin{array}{ccc|ccc} a_{11} & a_{12} & a_{13} & 0 & 0 & 0 \\ a_{21} & a_{22} & a_{23} & 0 & 0 & 0 \\ a_{31} & a_{32} & a_{33} & 0 & 0 & 0 \\ \hline 1 & 0 & 0 & 0 & 0 & 0 \\ 0 & 1 & 0 & 0 & 0 & 0 \\ 0 & 0 & 1 & 0 & 0 & 0 \end{array}\right], \quad \bar{\mathbf{B}}_{curr} = \left[\begin{array}{ccc} b_{11} & b_{12} & b_{13} \\ b_{21} & b_{22} & b_{23} \\ b_{31} & b_{32} & b_{33} \\ \hline 0 & 0 & 0 \\ 0 & 0 & 0 \\ 0 & 0 & 0 \end{array}\right] \tag{A.15}$$

where the nested matrix coefficient blocks a_{ij} and b_{ij} correspond explicitly to the top-left 3×3 submatrices extracted from the full system matrices $\mathbf{A}_{cc}$ (or $\mathbf{A}_{cv}$) and $\mathbf{B}_u$, respectively.

A.4.2 Outer-Loop: SISO Input Voltage Control (2x2)

The slower outer loop manages the input capacitor voltage dynamics as an independent Single-Input Single-Output (SISO) state system $\dot{V}_{C_{in}}$. The total aggregated current demand generated by this stage acts as the control command sent directly down to the inner phase current tracking loops:

$$\bar{\mathbf{A}}_{volt,cc} = \begin{bmatrix} 0 & 0 \\ 1 & 0 \end{bmatrix}, \quad \bar{\mathbf{A}}_{volt,cv} = \begin{bmatrix} -\frac{1}{C_{in}R_{in}} & 0 \\ 1 & 0 \end{bmatrix}, \quad \bar{\mathbf{B}}_{volt} = \begin{bmatrix} -\frac{1}{C_{in}} \\ 0 \end{bmatrix} \tag{A.16}$$

A.5 Simplification Variables (σ)

The physical inverse inductance matrix mapping $\mathbf{L}_{abc}^{-1}(\theta)$ is explicitly evaluated by separating out the position-invariant denominator term σ_6. The analytical decoupling matrix expansion maps to:

$$\mathbf{L}_{abc}^{-1}(\theta) = \frac{1}{\sigma_6}\begin{pmatrix}\lambda_1 & \sigma_2 & \sigma_1\\ \sigma_2 & \lambda_2 & \sigma_3\\ \sigma_1 & \sigma_3 & \lambda_3\end{pmatrix} \tag{A.17}$$

where L_m is the machine mutual inductance, L_{ls} is the stator leakage inductance, L_δ is the saliency inductance amplitude, and p represents the total motor pole pair count. The internal geometric scaling variables are defined exactly by:

$$\lambda_1 = -3L_\delta^2 + 4\sigma_7 L_\delta L_{\text{ls}} + 4L_{\text{ls}}^2 + 8L_{\text{ls}}L_m + 3L_m^2 \tag{A.18}$$
$$\lambda_2 = -3L_\delta^2 - 4\sigma_4 L_\delta L_{\text{ls}} + 4L_{\text{ls}}^2 + 8L_{\text{ls}}L_m + 3L_m^2 \tag{A.19}$$
$$\lambda_3 = -3L_\delta^2 - 4\sigma_5 L_\delta L_{\text{ls}} + 4L_{\text{ls}}^2 + 8L_{\text{ls}}L_m + 3L_m^2 \tag{A.20}$$
$$\sigma_1 = -3L_\delta^2 - 4L_{\text{ls}}\sigma_5 L_\delta + 3L_m^2 + 2L_{\text{ls}}L_m \tag{A.21}$$
$$\sigma_2 = -3L_\delta^2 - 4L_{\text{ls}}\sigma_4 L_\delta + 3L_m^2 + 2L_{\text{ls}}L_m \tag{A.22}$$
$$\sigma_3 = -3L_\delta^2 + 4L_{\text{ls}}\sigma_7 L_\delta + 3L_m^2 + 2L_{\text{ls}}L_m \tag{A.23}$$

The angular modulation parameters represent spatial phase-shifting offsets defined as:

$$\sigma_4 = \cos\left(2p\theta - \tfrac{2\pi}{3}\right), \qquad \sigma_5 = \cos\left(2p\theta + \tfrac{2\pi}{3}\right), \qquad \sigma_7 = \cos(2p\theta) \tag{A.24}$$

The global determinant denominator scaling divisor σ_6 is physically evaluated by:

$$\sigma_6 = L_{\text{ls}}\left(-9L_\delta^2 + 4L_{\text{ls}}^2 + 12L_{\text{ls}}L_m + 9L_m^2\right) \tag{A.25}$$

B

Verification of Plant Model Linearisation

B.1 Three-Phase Operation

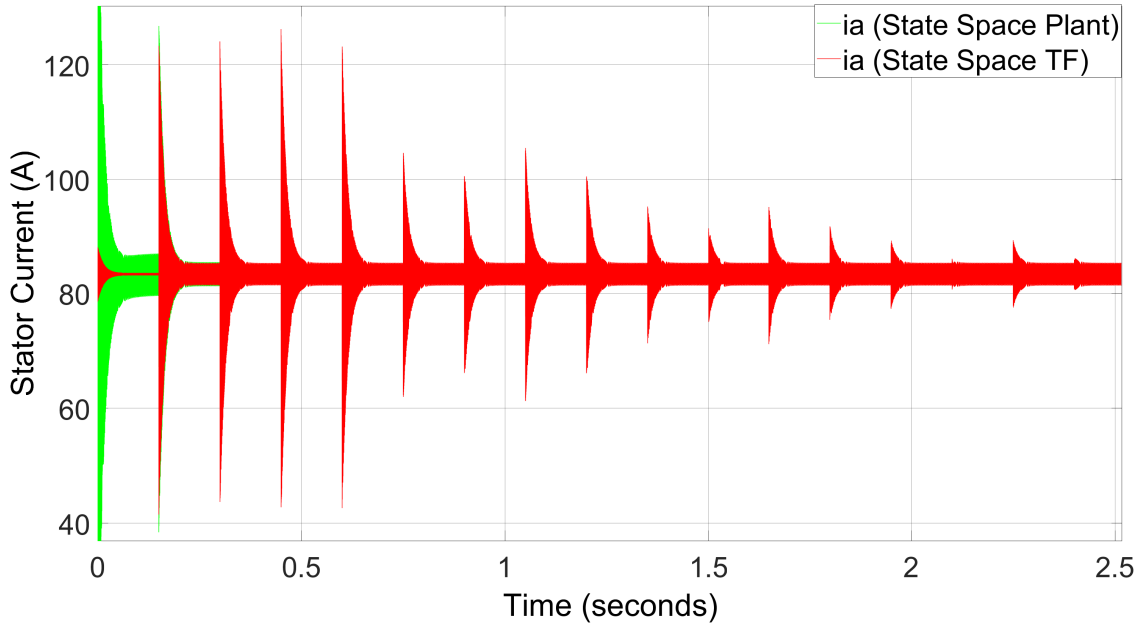

Figure B.1: Open-loop validation: linearised transfer function vs nonlinear state-space plant currents.

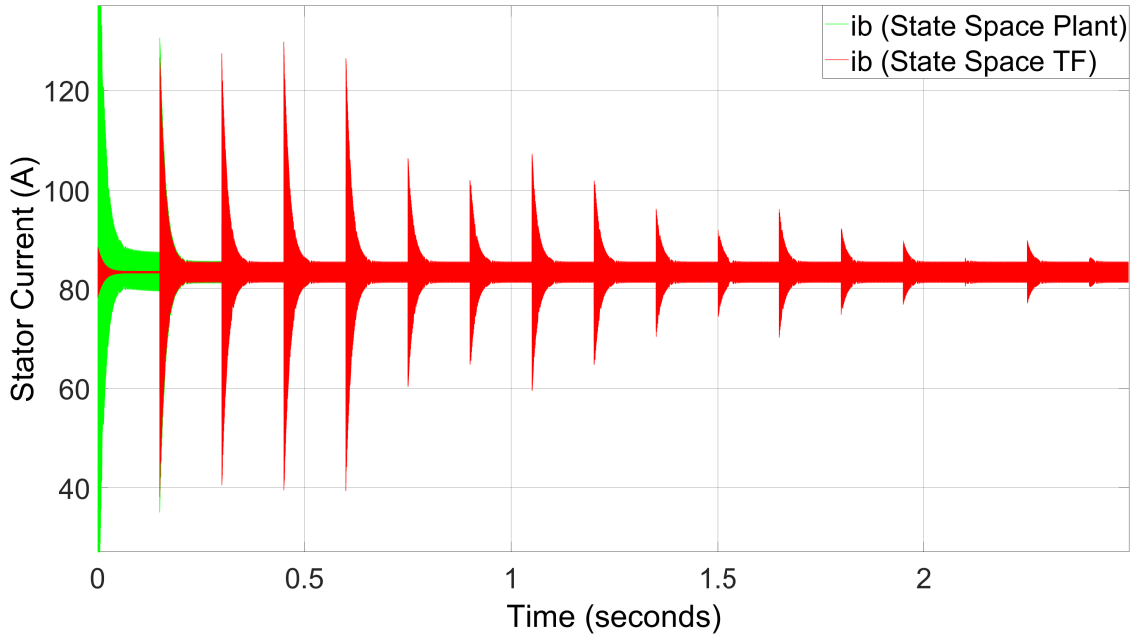

Figure B.2: Open-loop validation: linearised transfer function vs nonlinear state-space plant currents.

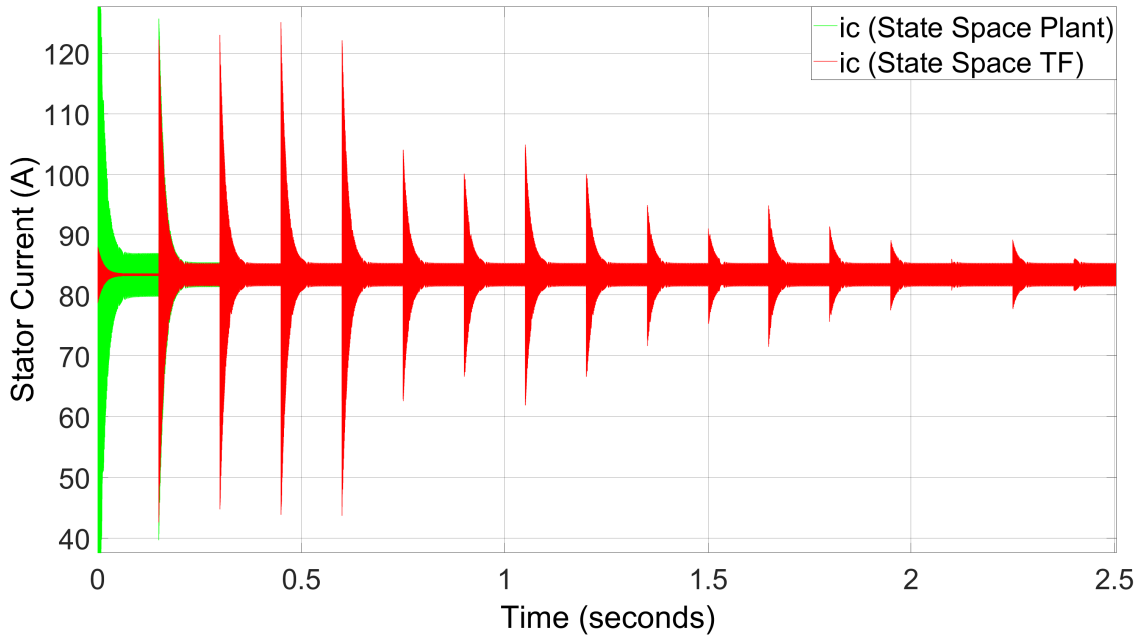

Figure B.3: Open-loop validation: linearised transfer function vs nonlinear state-space plant currents.

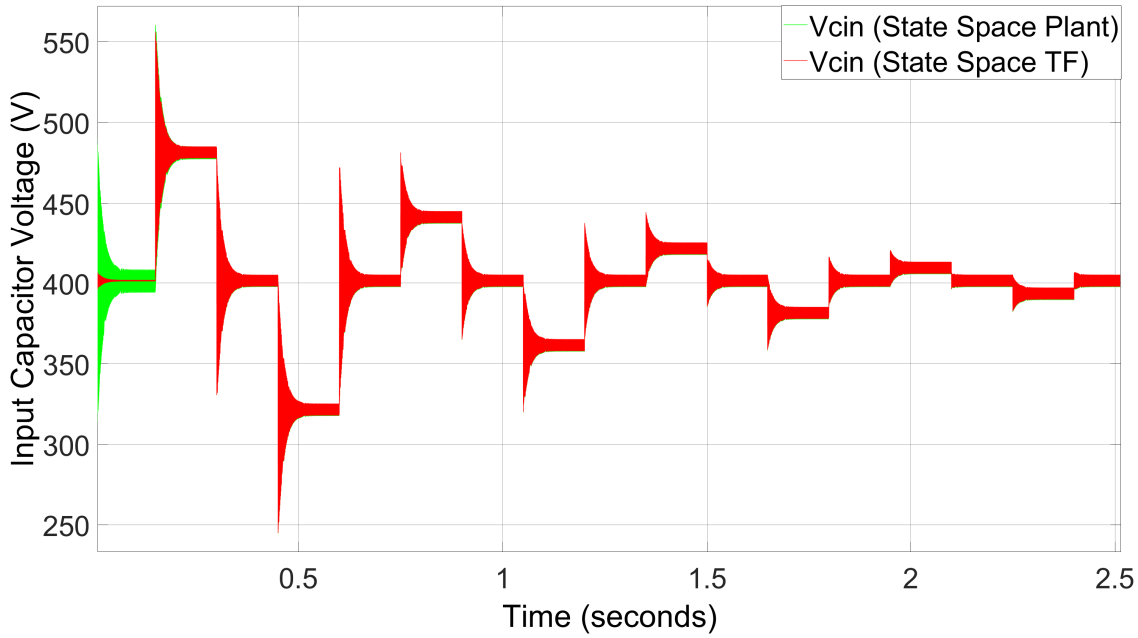

Figure B.4: Open-loop validation comparing the linearised transfer function with the nonlinear state-space plant for input voltage dynamics.

C

Plant Model Validation

C.1 Three-phase operation

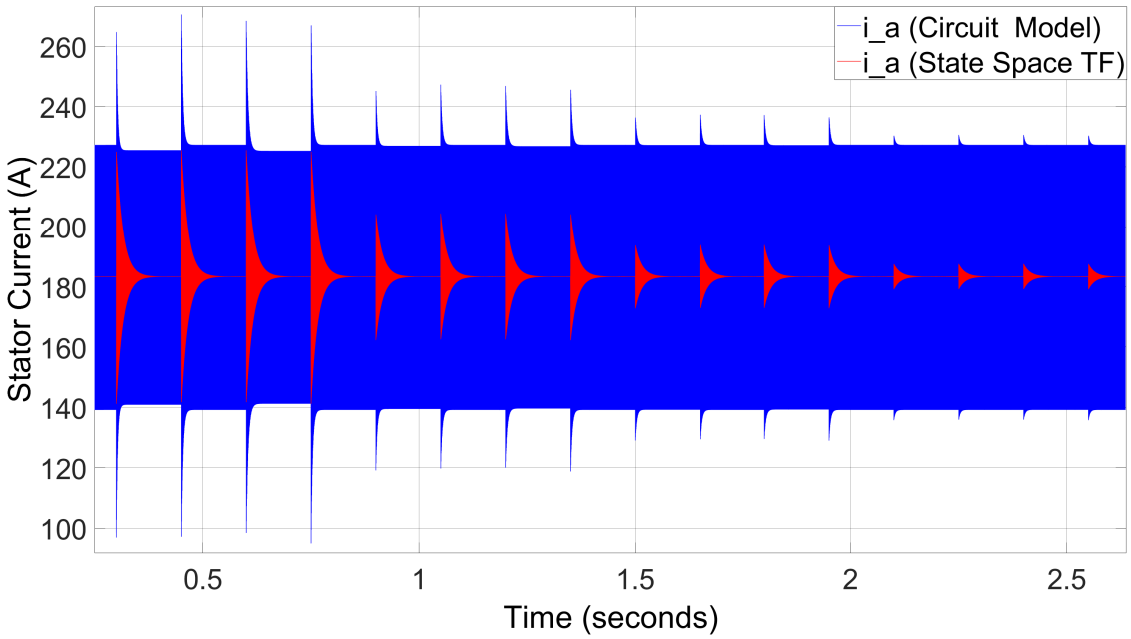

Figure C.1: Phase-A stator current response: state-space transfer function model versus circuit model.

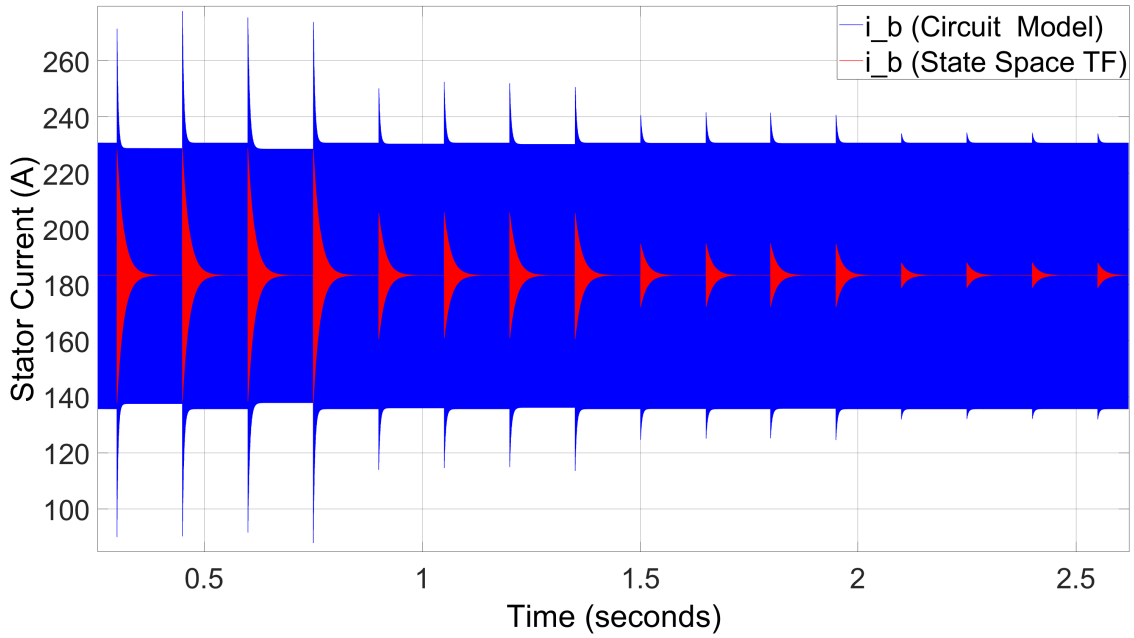

Figure C.2: Phase-B stator current response: state-space transfer function model versus circuit model.

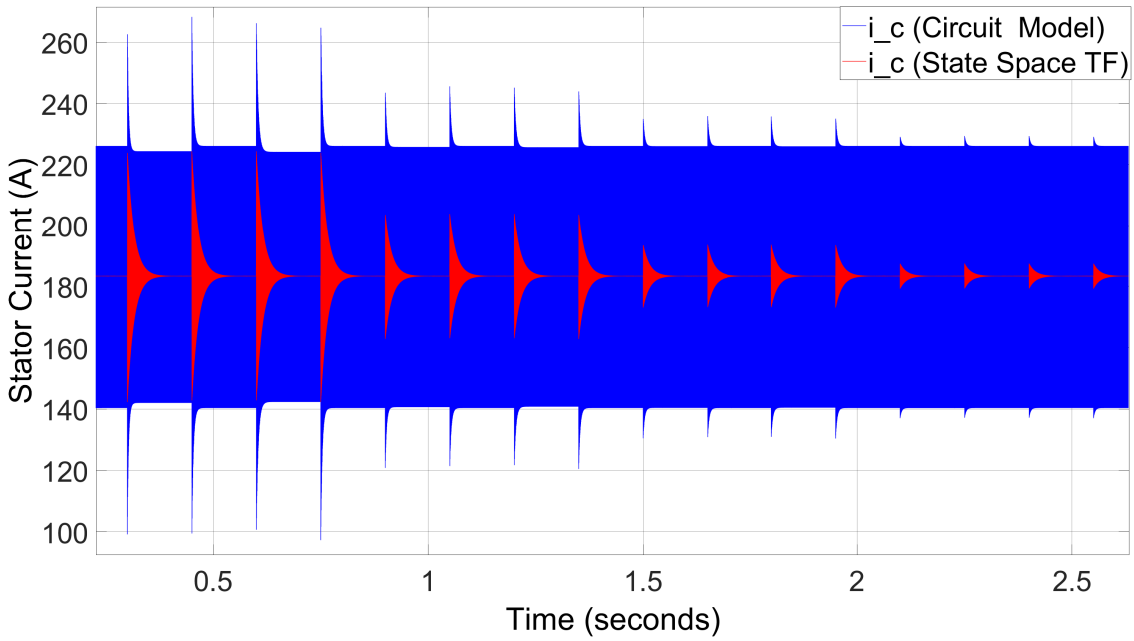

Figure C.3: Phase-C stator current response: state-space transfer function model versus circuit model.

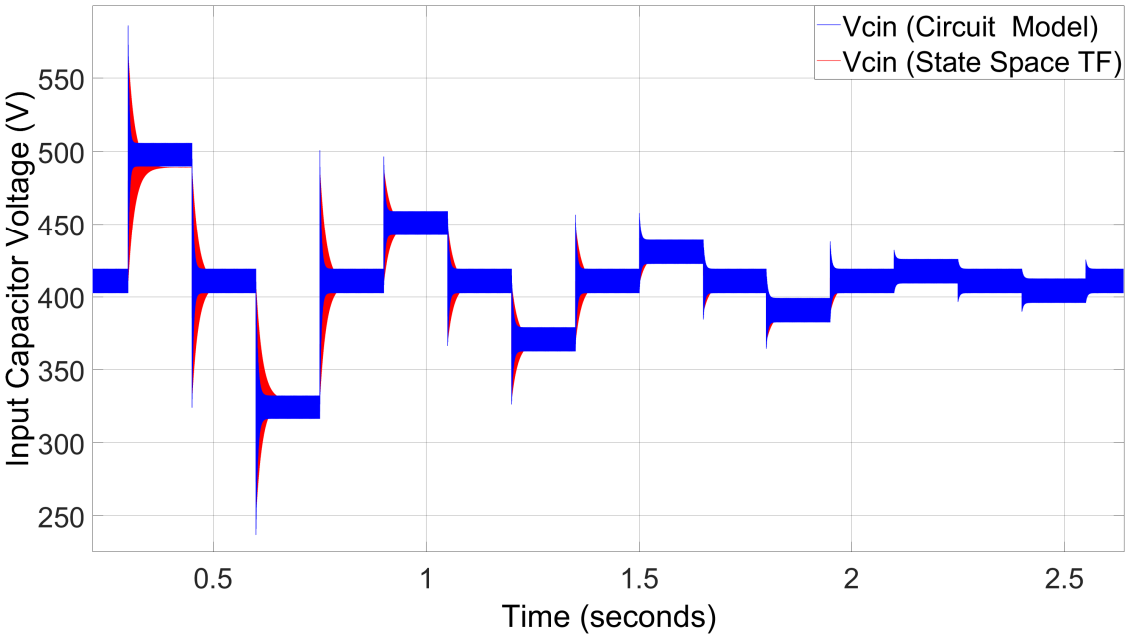

Figure C.4: Input capacitor voltage response for the state-space and circuit models

C.2 Two-phase operation

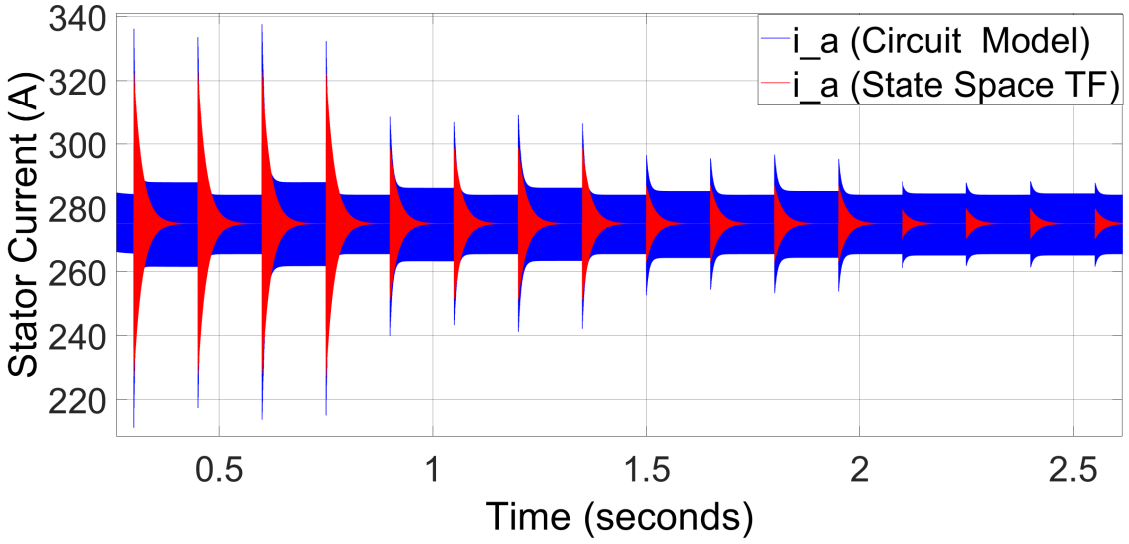

Figure C.5: Phase-A stator current response: state-space transfer function model versus circuit model.

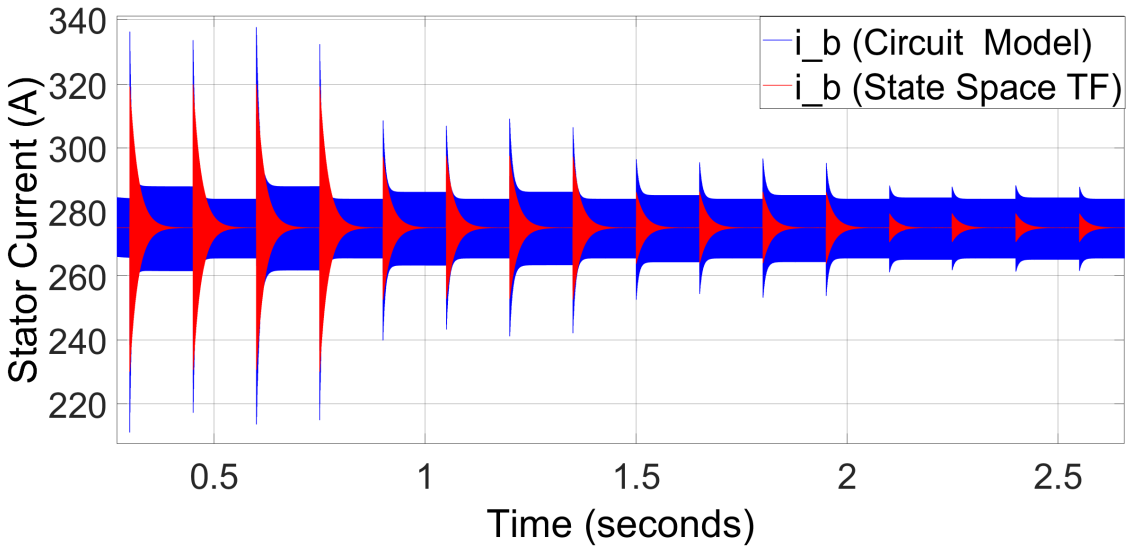

Figure C.6: Phase-B stator current response: state-space transfer function model versus circuit model.

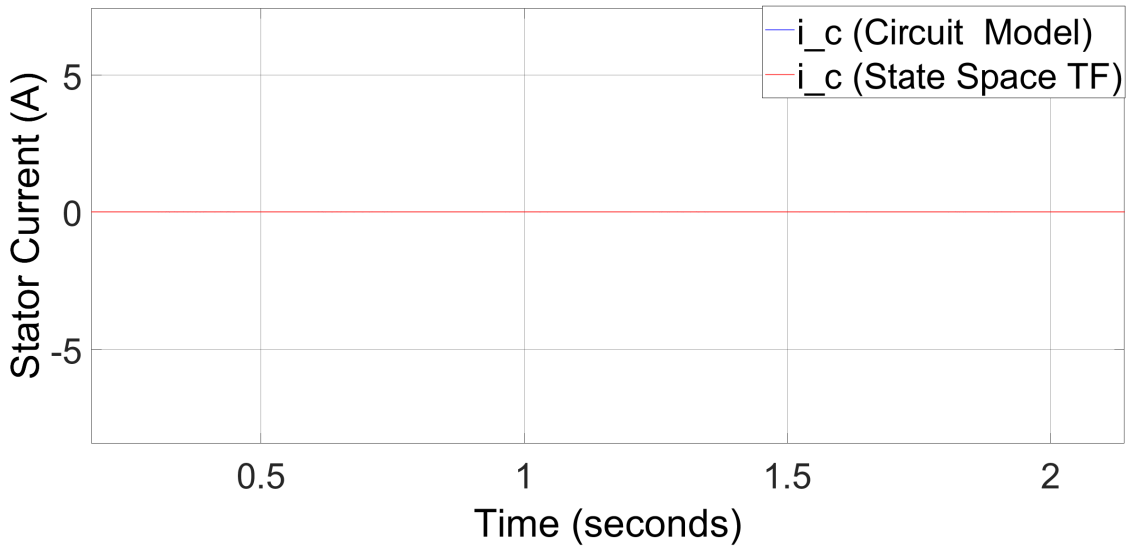

Figure C.7: Phase-C stator current response: state-space transfer function model versus circuit model.

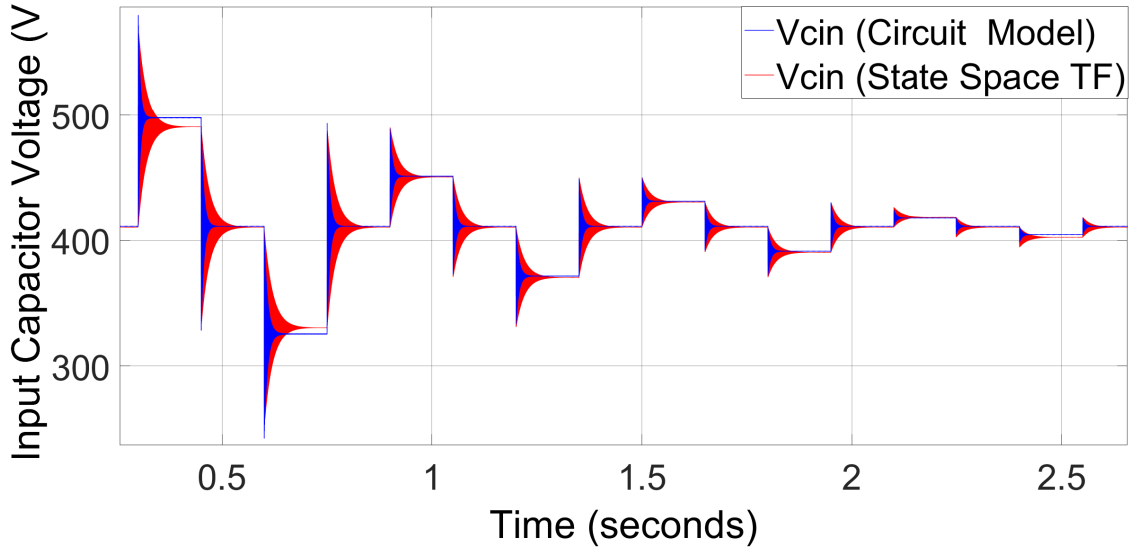

Figure C.8: Input capacitor voltage response for the state-space and circuit models

C.3 Single-phase operation

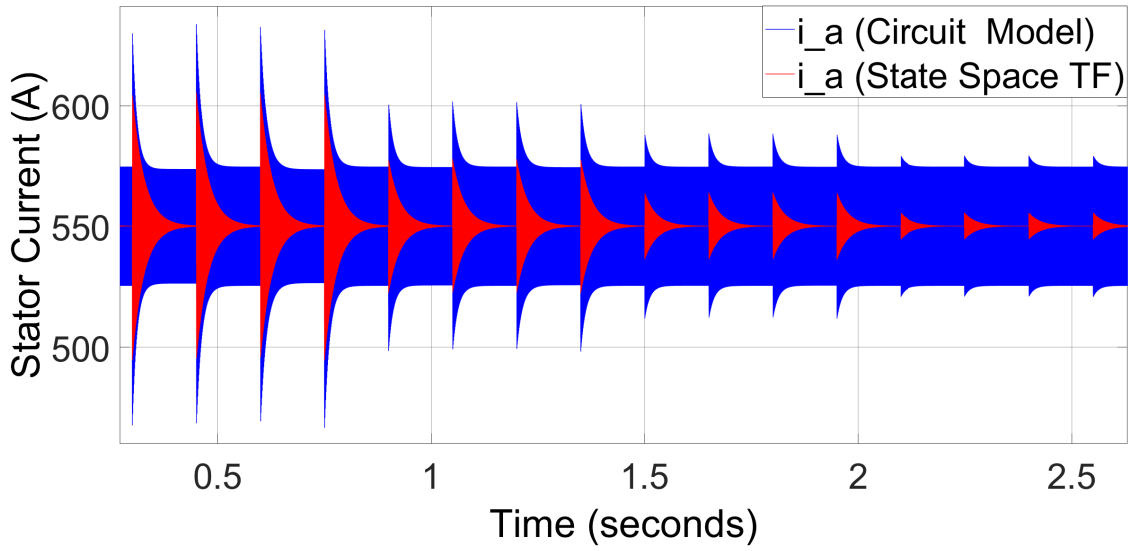

Figure C.9: Phase-A stator current response: state-space transfer function model versus circuit model.

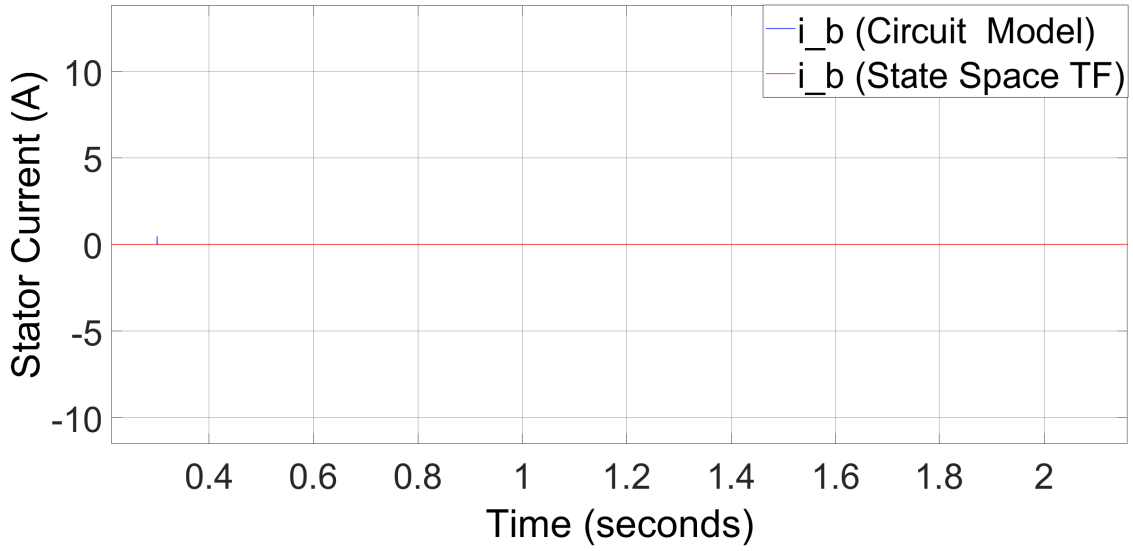

Figure C.10: Phase-B stator current response: state-space transfer function model versus circuit model.

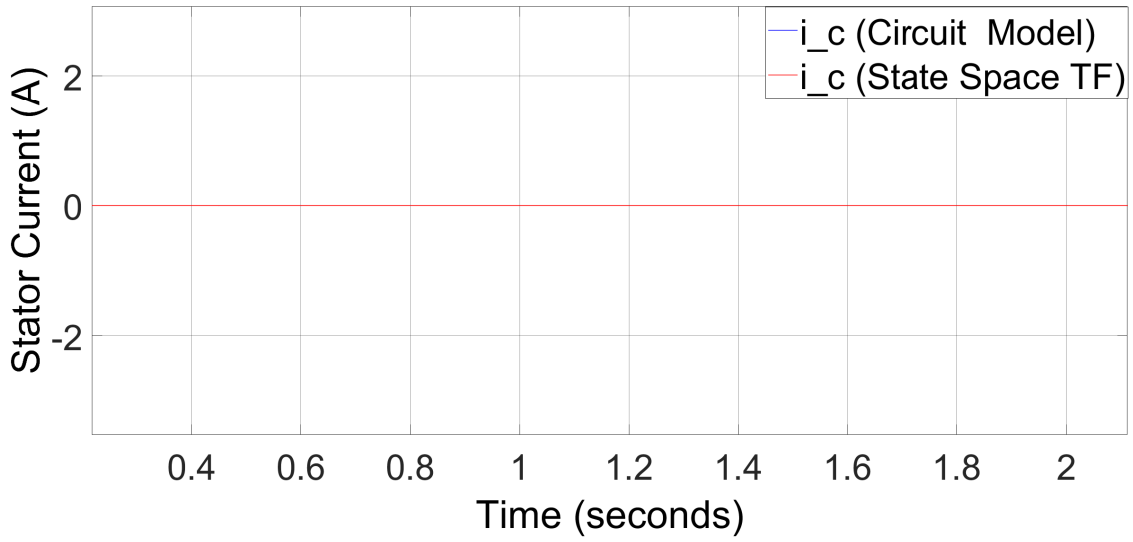

Figure C.11: Phase-C stator current response: state-space transfer function model versus circuit model.

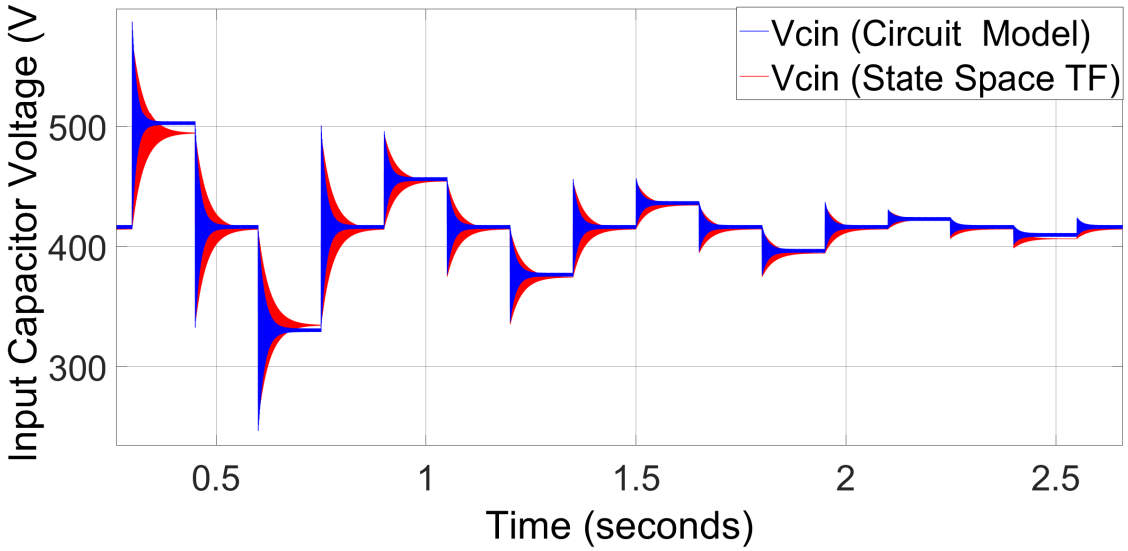

Figure C.12: Input capacitor voltage response for the state-space and circuit models.

D

MATLAB Implementation

D.1 Plant

```
function [dia_dt, dib_dt, dic_dt, dVCin_dt, d_active] = booster_plant(...
i_abc, V_Cin, d_abc)
%% Data
%%% MACHINE PARAMETERS (high frequency, 10 kHz)
L_m      = 50e-6;         % Mutual inductance              [H]
L_ls     = 75e-6;         % Leakage inductance             [H]
L_delta = 40e-6;          % Saliency reference              [H]
p        = 4;             % Pole pairs                     [-]
r_s      = 0.009;         % Stator winding resistance      [Ohm]
flux_m   = 0.04;          % PM flux linkage reference       [Wb]
%%% Angle dependent induction matrix %%%
r_angle    = deg2rad(0); % Rotor angle mechanical          [rad]
    basline is 30

% The "Paper Method" Equation 7
alpha = (3*L_m^2 - 3*L_delta^2)/L_ls + 2*L_m;
alpha_plus = 3*alpha + 4*L_ls + 6*L_m;
B11 = alpha_plus - 2*alpha + 4*L_delta*cos(2*p*r_angle);
B12 = alpha + 4*L_delta*cos(2*p*r_angle - 2*pi/3);
B13 = alpha + 4*L_delta*cos(2*p*r_angle + 2*pi/3);
B22 = alpha_plus - 2*alpha + 4*L_delta*cos(2*p*r_angle + 2*pi/3);
B23 = alpha + 4*L_delta*cos(2*p*r_angle);
B33 = alpha_plus - 2*alpha + 4*L_delta*cos(2*p*r_angle - 2*pi/3);
B = (1/(L_ls * alpha_plus)) * [B11 B12 B13;
                               B12 B22 B23;
                               B13 B23 B33];
L_inv_smart =  B;
%%% Angle dependent induction matrix %%%

V_battery = 800;          % Battery terminal voltage       [V]
I_station = 450;          % Constant station current       [V]
C_in      = 2e-3;  % Input capacitor                [A]
r_s      = 0.009;         % Stator winding resistance      [Ohm]

num_phases_active = 3; % Has to be 3!

% 0. Ensure inputs are column vectors
i_vec = i_abc(:);
```

```
    d_vec = d_abc(:);

    % 1. Create an active phase mask
    % This ensures i_c = 0 and d_c = 0 if num_phases_active is 2
    mask = zeros(3,1);
    mask(1:num_phases_active) = 1;

    i_active = i_vec .* mask;
    d_active = d_vec .* mask;

    %% 2. Inductor KVL (Averaged)
    % vL calculation for each phase
    vL = V_Cin - (1 - d_active) .* V_battery - r_s * i_active;

    % Derivative calculation using pre-calculated inverse
    % Inactive rows in L_inv_smart are 0, so di_dt for inactive
       phases will be 0.
    di_dt = L_inv_smart * vL;

    %% 3. Input Capacitor KCL (Averaged)
    % I_station flows in, sum of inductor currents flows out
    dVCin_dt  = (1 / C_in) * (I_station - sum(i_active));

    %% 5. Mapping outputs
    dia_dt = di_dt(1);
    dib_dt = di_dt(2);
    dic_dt = di_dt(3);
end
```

D.2 Script

```
%DC-DC Boost Control
%Chalmers : Abukar Hassan
%Good to know: Simulating switching at 10 kHz, my simulation max
   step size should be at least 1 microsecond.
%Define the Parameters
%[1] Y. Hwang, J. Kim, J. Choi and K. Nam,
%"Phase Current Equalisation Method of IPMSM-Based on-Board Boost
   Converter
%for Electric Vehicles," *IEEE*, 202X.
%% MACHINE PARAMETERS (high frequency, 10 kHz)
L_m     = 50e-6;        % Mutual inductance             [H]
L_ls    = 75e-6;        % Leakage inductance            [H]
L_delta = 40e-6;        % Saliency reference             [H]
p       = 4;            % Pole pairs                    [-]
r_s     = 0.009;        % Stator winding resistance     [Ohm]
flux_m  = 0.04;         % PM flux linkage reference      [Wb]

%% SYSTEM PARAMETERS
v_station = 400;        % Charger input voltage         [V]
v_battery = 800;        % Battery terminal voltage      [V]
P_station = 200e3;      % Nominal charging power        [W]
eta       = 0.94;       % Efficiency                    [-]
```

```
21
22 C_in      = 2e-3;  % Input capacitor               [F]
23 C_out     = 5e-3;    % Output capacitor              [F]
24 R_in      = 0.01;       % Input cable + connector       [Ohm]
25 R_out     = 0.01;       % DC link cable to battery      [Ohm]
26 I_station = 450;        % Station Current               [A]
27
28 %% SWITCHING PARAMETERS
29 f_sw      = 10e3;       % Switching frequency           [Hz]
30 T_s       = 1/f_sw;     % Switching period              [s]
31 I_max_sw  = 250;        % Switch current limit          [A]
32
33 %% ROTOR ANGLE
34 r_angle   = deg2rad(30); % Rotor angle mechanical        [rad]
35                          % 7.5 mech = 30 elec deg (p=4)
36
37 %% PHASE SELECTION
38 % Change this to 1, 2, or 3 to send current though number of phase
39 num_phases_active = 3;
40
41
42 ia_steady = I_station / num_phases_active;
43 ib_steady = (num_phases_active >= 2) * ia_steady;
44 ic_steady = (num_phases_active >= 3) * ia_steady;
45
46 %% PHASE SELECTION
47 x1_e= I_station/3; %Current reference, Phase A
48 x2_e= I_station/3; %Current reference, Phase B
49 x3_e= I_station/3; %Current reference, Phase C
50
51 x4_e=v_station ; %Voltage reference, Input Capacitor Voltage
52 u_e=[0.5;
53     0.5;
54     0.5];
55 Operating Point & Phase Selection
56 num_phases_active = 3;   % Options: 1, 2, or 3 phases
57
58 % Steady-state current per phase
59 ia_steady = I_station / num_phases_active;
60 ib_steady = (num_phases_active >= 2) * ia_steady;
61 ic_steady = (num_phases_active >= 3) * ia_steady;
62
63 % Equilibrium Duty Cycle (de) including resistive drops
64 %Vcin_steady = (1 - de) * v_battery + r_s * ia_steady;
65 Vcin_ss = v_station - (I_station * R_in);
66 Vout_ss = v_battery + (I_station * 0.94 * (v_station/v_battery)) *
       R_out;
67 de = 1 - (Vcin_ss - r_s * ia_steady) / Vout_ss;
68
69 %Vcin_steady = (1 - de) * v_battery + r_s * ia_steady;
70 Leveraging Matlab Symbolic
71 %% 1. SYMBOLIC VARIABLE DEFINITIONS
72 % Using 'real' helps MATLAB simplify complex expressions
73 %syms L_m L_ls L_delta p r_angle r_s flux_m
74 %syms v_station v_battery C_in C_out R_in R_out I_station
75 %syms de s
```

```
76
77  The Rotor Angle Dependent Induction Matrix
78  %% Construct the Fixed Inductance Matrix  L_abc
79  L_abc = [L_m + L_ls,  -L_m/2,      -L_m/2;
80           -L_m/2,       L_m + L_ls, -L_m/2;
81           -L_m/2,      -L_m/2,       L_m + L_ls]
82
83  %%Construct the Saliency Matrix L_rlc
84  % Define the time-varying components
85  c1 = cos(2*p*r_angle);
86  c2 = cos(2*p*r_angle - 2*pi/3);
87  c3 = cos(2*p*r_angle + 2*pi/3);
88
89  L_rlc_angle = L_delta * [c1, c2, c3;
90                           c2, c3, c1;
91                           c3, c1, c2];
92
93  %% Construct the real inductance matrix L_abc(angle),
94  % which represents the rotor angle dependent inductance of the
        stator windings
95  L_abc_angle = L_abc - L_rlc_angle;
96  % The flux linkage does not affect the Change in Current.
97  %Since ÏĹ_m represents the back electromotive force (EMF) and the
        electric machine rotor is stationary, dÏĹ(angle)/dt = 0.
98  flux_linkage = flux_m * [cos(p*r_angle);
99  cos(p*r_angle - 2*pi/3);
100 cos(p*r_angle +  2*pi/3)];
101 The Voltage over the E-Machine Copper Coil (V_L)
102 V_L = r_s * i_abc + d(L_abc_angle * i_abc + flux_linkage) / dt
103 %Analytical Inverse of inductance matrix (The "Paper Method")
104 % Definitions from Equation 7
105 alpha = (3*L_m^2 - 3*L_delta^2)/L_ls + 2*L_m;
106 alpha_plus = 3*alpha + 4*L_ls + 6*L_m;
107
108 % Elements of the Inverse Matrix (B matrix)
109 B11 = alpha_plus - 2*alpha + 4*L_delta*cos(2*p*r_angle);
110 B12 = alpha + 4*L_delta*cos(2*p*r_angle - 2*pi/3);
111 B13 = alpha + 4*L_delta*cos(2*p*r_angle + 2*pi/3);
112 B22 = alpha_plus - 2*alpha + 4*L_delta*cos(2*p*r_angle + 2*pi/3);
113 B23 = alpha + 4*L_delta*cos(2*p*r_angle);
114 B33 = alpha_plus - 2*alpha + 4*L_delta*cos(2*p*r_angle - 2*pi/3);
115
116 % Construct Analytical  B matrix
117 B_matrix = (1/(L_ls * alpha_plus)) * [B11 B12 B13;
118                                       B12 B22 B23;
119                                       B13 B23 B33];
120
121 %L_angle_inv = simplify(B_matrix) or pretty(B_matrix)
122 L_angle = L_abc_angle
123 L_angle_inv = B_matrix
124
125 sum(L_angle_inv(:,1))
126 sum(L_angle_inv(:,2))
127 sum(L_angle_inv(:,3))
128 Dynamic Induction for Given Phase Number of Phase
129 L_inv_smart = zeros(3,3);
```

```
130
131
132 switch num_phases_active
133     case 3
134         % The "Paper Method" Equation 7
135         alpha = (3*L_m^2 - 3*L_delta^2)/L_ls + 2*L_m;
136         alpha_plus = 3*alpha + 4*L_ls + 6*L_m;
137         B11 = alpha_plus - 2*alpha + 4*L_delta*cos(2*p*r_angle);
138         B12 = alpha + 4*L_delta*cos(2*p*r_angle - 2*pi/3);
139         B13 = alpha + 4*L_delta*cos(2*p*r_angle + 2*pi/3);
140         B22 = alpha_plus - 2*alpha + 4*L_delta*cos(2*p*r_angle + 2*
                pi/3);
141         B23 = alpha + 4*L_delta*cos(2*p*r_angle);
142         B33 = alpha_plus - 2*alpha + 4*L_delta*cos(2*p*r_angle - 2*
                pi/3);
143         B = (1/(L_ls * alpha_plus)) * [B11 B12 B13;
144                                        B12 B22 B23;
145                                        B13 B23 B33];
146         L_inv_smart =  B
147         phase_3_test= inv(L_angle)
148
149     case 2
150         % Analytical 2x2 inverse for Phases A and B
151         L_sub = L_angle(1:2, 1:2);
152         det_L = L_sub(1,1)*L_sub(2,2) - L_sub(1,2)*L_sub(2,1);
153         L_inv_smart(1:2, 1:2) = (1/det_L) * [L_sub(2,2), -L_sub
                (1,2);
154         -L_sub(2,1), L_sub(1,1)]
155         phase_2_test= inv(L_angle(1:2, 1:2))
156
157     case 1
158         % Scalar inverse for Phase A
159         L_inv_smart(1,1) = 1 / L_angle(1,1)
160         phase_1_test= inv(L_angle(1:1))
161 end
162 %The Oscillation Frequency Corresponds to the Natural RLC Resonance
        Frequency of the System.
163 %Resonant frequency formula
164 L_eq = sum(L_angle(:,1));
165 C_eq = C_in;
166 R_eq = r_s;
167
168 omega_0 = 1 / sqrt(L_eq * C_eq);
169
170 alpha = R_eq / (2 * L_eq);
171
172 omega_d = sqrt(omega_0^2 - alpha^2);
173
174 f_n = omega_d / (2*pi) % Resonant frequency
175
176 delta_t_scope = 0.002% Peak to Peak, time [s]
177 f_n_scope = 1/delta_t_scope
178 %Simple Efficiency Estimation Based on Voltage Drop
179 %% DYNAMIC PHYSICAL ETA CALCULATION
180 Pin = v_station * I_station;
181
```

```
% 1. Input Side Loss
Loss_in = I_station^2 * R_in;

% 2. Converter/Machine Loss (3 phases)
Loss_conv = num_phases_active * (ia_steady^2 * r_s);

% 3. Output Side Loss
% Estimate I_out based on conservation of energy (Pin/Vbat)
I_out_est = Pin / v_battery;
Loss_out = I_out_est^2 * R_out;

% 4. Total Physical Loss
Total_Loss = Loss_in + Loss_conv + Loss_out;

% 5. Measured Efficiency
eta_physical = (Pin - Total_Loss) / Pin;

% Overwrite the static variable
eta = eta_physical;
Duty Calculation with Resistance
V_bat = (1/(1-d))*(V_station -  r_s * ia_steady) ;
d = 1 -  ( (V_station - r_s * ia_steady)  / V_bat )
% Calculate the actual voltage at the Input Capacitor
Vcin_steady = v_station - (I_station * R_in);

% Calculate the actual voltage at the Output (before R_out)
Vout_steady = v_battery + (I_station * eta * (v_station/v_battery))
    * R_out;

% Recalculate de with these physical drops
de = 1 - (Vcin_steady - r_s * ia_steady) / Vout_steady;
Average State-Space Model of the Boost Converter
%% DYNAMIC LINEARISATION
% 0. Operating Point Variables
de = 1 - (v_station - r_s * ia_steady) / v_battery;
v_battery_e = v_battery
active_mask = (1:3) <= num_phases_active;
M = diag(active_mask); % 3x3 Diagonal mask for control inputs

%% 1. Construct A Matrix (4x4)
% Top-Left: Inductor Resistance (L_inv_smart handles zeros for
    inactive phases)
A_tl = -L_inv_smart * r_s;

% Top-Right: How V_Cin affects current
% In KVL: L*di/dt = V_Cin - (1-d)V_batt... Derivative w.r.t V_Cin
    is 1.
A_tr = L_inv_smart * ones(3,1);

% Bottom-Left: How phase currents affect V_Cin
% dVCin/dt = (1/Cin) * (I_station - sum(i_active)).
Derivative w.r.t i_abc is -1/Cin.
A_bl = (-1 / C_in) * active_mask;

% Bottom-Right: Capacitor/Station Damping
A_br = 0;
```

```
235
236
237 % Final A Matrix (4 rows, 4 columns)
238 A_av_lin = [A_tl, A_tr;
239             A_bl, A_br]
240
241 %% 2. Construct B Matrix (4x5)
242 % Columns 1-3: Control Inputs [da, db, dc]
243 % Derivative of L*di/dt = -(1-d)V_batt w.r.t 'd' is +V_batt.
244 B_duty = (L_inv_smart * v_battery_e) * M;
245 B_duty_bottom = zeros(1, 3);
246
247 % Column 4: V_station (Input Disturbance)
248 B_vstat_top = zeros(3, 1);
249 B_Istat_bottom = 1 / C_in;
250
251 % Column 5: V_battery (Input Disturbance)
252 % Derivative of -(1-d)V_batt w.r.t V_batt is (d-1).
253 B_vbatt_top = L_inv_smart * ones(3,1) * (de - 1);
254 B_vbatt_bottom = 0;
255
256
257 % Final B Matrix (4 rows, 5 columns)
258 B_av_lin = [ B_duty,          B_vstat_top,    B_vbatt_top ;
259              B_duty_bottom,  B_Istat_bottom, B_vbatt_bottom ]
260
261 % Final C Matrix (4 rows, 4 columns)
262 C_av_lin = [1 0 0 0;
263     0 1 0 0;
264 0 0 1 0;
265 0 0 0 1;]
266 Reachability (Controllability) Test
267 % The Reachability Matrix
268 Co = ctrb(A_av_lin, B_av_lin);
269
270 % Check the rank
271 rank_Co = rank(Co) % Should be 4
272 %is_controllable = (rank_Co == size(A_av_lin, 1))
273 Observability Test
274 % The Observability Matrix
275 Wo = obsv(A_av_lin, C_av_lin);
276
277 % Check the rank
278 rank_Wo = rank(Wo)
279 %is_observable = (rank_Wo == size(A_av_lin, 1)) % Should be 4
280 Transfer Function
281 G(s) = C(sI - A)^{-1}B
282 %% Transfer Functions (equal interleaved duty assumption)
283 B_equal = sum(B_av_lin(:, 1:3), 2)   % 4x1, valid since da=db=dc=d
284
285 % Define the C matrix to get only Vout (the 4th state)
286 C_vout = [1 0 0 0];
287 D_single = 0
288
289 %syms s % Define Laplace variable
290
```

```
% 1. Create the Symbolic Identity Matrix
%I_mat = eye(size(A_av_lin, 1));

% 2. Calculate the Symbolic Transfer Function
% Formula: G(s) = C * inv(s*I - A) * B
% We use 'simplify' to clean up the resulting polynomial
%G_sym = C_vout * inv(s*I_mat - A_av_lin) * B_equal;

% 3. Clean and Display
%G_sym = simplify(G_sym)
%pretty(G_sym) % Displays it in a readable math format


% Create the Transfer Function
[num, den] = ss2tf(A_av_lin, B_equal, C_vout, D_single);
G_vout_dall = tf(num, den)


% B matrix check
1/(C_in*R_in)
- sum(L_inv_smart(:,1))*(1-de)
Bode Plot for Stability Margin Evaluation
We evaluate the stability margins using one of the current loops
A_i = A_av_lin(1:3,1:3);
B_i = B_av_lin(1:3,1:3);

% Use Phase A as representative output
B_a = B_i(:,1);         % duty âĘŠ phase A current
C_a = [1 0 0];          % measure phase A current
D = 0;

sys_ia = ss(A_i, B_a, C_a, D);

figure
margin(sys_ia)
grid on
title('INNER LOOP: Duty âĘŠ Phase A Current')
%%Control Design (1): Kp and Ki Design Using LQR for the Current
    Loop
%System bandwidth is constrained by both stability margins and the
    switching frequency. To maintain robust performance, the fastest
     pole should be limited to one-fifth of the switching frequency.
     p1 âĽđ (2pi*f_sw)/5
%% Inner Loop - 3-Phase Current Control (3x3 MIMO)
% Extract the 3x3 current dynamics from the linear model
A_i = A_av_lin(1:3, 1:3);
B_i = B_av_lin(1:3, 1:3);
C_i = eye(3);

% Augment with 3 Integrators (one for each phase)
% States: [ia; ib; ic; int_ia; int_ib; int_ic]
A_inner = [A_i,           zeros(3,3);
          -C_i,        zeros(3,3)];
B_inner = [B_i;           zeros(3,3)];
C_inner = [C_i;           zeros(3,3)];

```

```
% Verify Controllability
%This must be 6 for the system to be stable/solvable
rank(ctrb(A_inner, B_inner))
poles_inner_org = eig(A_inner)


%% 3. Bryson's Rule Tuning

% Decrease Q to allow the current to react fast
max_i_err = 1;      % Diviation allowed
max_int_i = 1e-4;    % Very tight integral weight

% Decrease R to allow the duty cycle to react faster
max_d_move = 1e-4;     % Very tight duty weight

Q_i = diag([1/max_i_err^2, 1/max_i_err^2, 1/max_i_err^2, ...
            1/max_int_i^2, 1/max_int_i^2, 1/max_int_i^2]);
R_i = eye(3) * (1 / max_d_move^2);

%% 4. Solve LQR
K_lqr_inner = lqr(A_inner, B_inner, Q_i, R_i);

%% 5. Separate Gains for Simulink
Kp_i = K_lqr_inner(:, 1:3) % 3x3 Proportional Gain
Ki_i = K_lqr_inner(:, 4:6) % 3x3 Integral Gain (Matches 2
    integrators)

poles_inner = eig(A_inner - B_inner * K_lqr_inner)
real(poles_inner) % CHECK
%%Control Design (2): Kp and Ki Tuning Using Pole Placement for the
     Voltage Loop
%For proper time-scale separation, the voltage controller is
    designed to be 10x slower than the current controller.
%% Outer Loop - Capacitor Voltage Control (1x1 SISO)
% Plant: dVCin/dt = (1/C) * (I_station - I_sum)
% We treat I_sum as the control input 'u' for this loop.
A_v = 0; % Capacitor voltage is an integrator of current
B_v = -1 / C_in; % Negative because current flows OUT of Cin in
    your model
C_v = 1

% Augment with 1 Integrator for Voltage
A_outer = [A_v,  0;
          -C_v,    0]; % Tracking VCin
B_outer = [B_v;  0];

% Verify Controllability
%This must be 2 for the system to be stable/solvable
rank(ctrb(A_outer, B_outer))
poles_org = eig(A_outer)

% % Define poles: 10ÃÙ slower settling time than current loop
% Get your closed-loop current poles
poles_inner_gain = real(poles_inner(1:3))
poles_inner_integral = real(poles_inner(4:5))

```

```
395
396 % 2 Poles total
397 desired_outer_poles = [max(poles_inner_gain)*2, max(
        poles_inner_integral)*4];
398
399 % Calculate Gains (SISO - returns scalars)
400 k_outer = place(A_outer, B_outer, desired_outer_poles);
401
402 Kp_v = k_outer(1); % Proportional gain for voltage
403 Ki_v = k_outer(2); % Integral gain for voltage
404
405 % Calculate the closed-loop A matrix
406 A_cl_outer = A_outer - B_outer * k_outer;
407
408 % Get the eigenvalues (poles)
409 poles = eig(A_cl_outer)
```

D.3 Current Correction in Three-Phase PWM Interleaved Systems

The proposed correction approach is based on phase-dependent compensation terms derived from machine parameters and operating conditions. The current correction function, which is provided in the Appendix, implements this principle by adjusting the measured phase currents as follows:

$$i_{x,\text{corr}} = i_x + Q_x \tag{D.1}$$

where Q_x represents a phase-dependent correction term dependent on duty cycle, rotor angle, and machine inductances.
The implementation is summarised in the following function:

```
1  function [ia_corr, ib_corr, ic_corr] = Q_correction(ia, ib, ic, d,
       theta)
2      % High-frequency values from Table 1
3      %[1] Y. Hwang, J. Kim, J. Choi and K. Nam, âĂŸPhase Current
           Equalization
4      Method of IPMSM-Based on-Board Boost Converter
5      for Electric Vehicles,âĂİ *IEEE*, 202X.
6
7      L_m      = 50e-6;         % Mutual inductance              [H]
8      L_ls     = 75e-6;         % Leakage inductance             [H]
9      L_delta = 40e-6;          % Saliency reference              [H]
10     p          = 4;           % Pole pairs                     [-]
11     f_sw       = 10e3;        % Switching frequency            [Hz]
12     T_s        = 1 / f_sw;    % Sampling time                  [s]
13     V_chr      = 400;         % Charging station voltage       [V]
14
15     alpha       = (3*L_m^2 - 3*L_delta^2)/L_ls + 2*L_m;
16     alpha_plus = 3*alpha + 4*L_ls + 6*L_m;
17
18     K_Q = (2 * V_chr * T_s * L_delta) / (sqrt(3) * L_ls *
           alpha_plus);
```

```
19
20      if d < 1/3
21          Q_scale = d / (1 - d);
22      elseif d < 2/3
23          Q_scale = (1 - 2*d) / (1 - d);
24      else
25          Q_scale = -1;
26      end
27
28      theta_a = theta;
29      theta_b = theta + pi/(3*p);
30      theta_c = theta - pi/(3*p);
31
32      Q_a = K_Q * Q_scale * sin(2 * theta_a);
33      Q_b = K_Q * Q_scale * sin(2 * theta_b);
34      Q_c = K_Q * Q_scale * sin(2 * theta_c);
35
36      ia_corr = ia + Q_a;
37      ib_corr = ib + Q_b;
38      ic_corr = ic + Q_c;
39  end
```

DEPARTMENT OF ELECTRICAL ENGINEERING
CHALMERS UNIVERSITY OF TECHNOLOGY
Gothenburg, Sweden
www.chalmers.se

CHALMERS
UNIVERSITY OF TECHNOLOGY